

# AI-Based Reconstruction for Fast MRI—A Systematic Review and Meta-Analysis

*This article provides a systematic review and the first meta-analysis to summarize the development of deep-learning-based compressed sensing-magnetic resonance imaging.*

By YUTONG CHEN, CAROLA-BIBIANE SCHÖNLIEB, PIETRO LIÒ<sup>ID</sup>, TIM LEINER<sup>ID</sup>, PIER LUIGI DRAGOTTI<sup>ID</sup>, *Fellow IEEE*, GE WANG<sup>ID</sup>, *Fellow IEEE*, DANIEL RUECKERT<sup>ID</sup>, *Fellow IEEE*, DAVID FIRMIN, AND GUANG YANG<sup>ID</sup>, *Senior Member IEEE*

**ABSTRACT** | Compressed sensing (CS) has been playing a key role in accelerating the magnetic resonance imaging (MRI) acquisition process. With the resurgence of artificial intelligence, deep neural networks and CS algorithms are being integrated to redefine the state of the art of fast MRI. The past several years have witnessed substantial growth in the

complexity, diversity, and performance of deep-learning-based CS techniques that are dedicated to fast MRI. In this meta-analysis, we systematically review the deep-learning-based CS techniques for fast MRI, describe key model designs, highlight breakthroughs, and discuss promising directions. We have also introduced a comprehensive analysis framework and a classification system to assess the pivotal role of deep learning in CS-based acceleration for MRI.

**KEYWORDS** | Compressed sensing (CS); deep learning; magnetic resonance imaging (MRI); neural network.

## I. INTRODUCTION

Magnetic resonance imaging (MRI) is a state-of-the-art medical imaging technique that can determine the structural and functional status of body tissues and organs [1]. However, the prolonged MRI acquisition time [2], [3] increases the scanning cost and limits its use in emergency settings. Moreover, subjects have to lie still in the scanners and even hold their breath for thoracic or abdominal imaging [1]. Hence, the slow acquisition of magnetic resonance (MR) images presents a significant inconvenience to patients and healthcare systems alike.

The reason for the slow MR acquisition rate is that, unlike other imaging modalities, e.g., X-ray and CT, MR data are acquired in the k-space. The k-space is related to the image domain via the Fourier transform [1], [4] and represents the spatial frequency information. During MRI acquisition, measures in the k-space are taken sequentially rather than simultaneously, thus prolonging the scanning time.

To address this limitation, the k-space can be undersampled, i.e., not sampled entirely. The missing k-space data

---

Manuscript received April 27, 2021; revised December 5, 2021; accepted December 20, 2021. Date of current version February 3, 2022. This work was supported in part by the British Heart Foundation under Project TG/18/5/34111 and Project PG/16/78/32402; in part by the European Research Council Innovative Medicines Initiative, DRAGON, under Grant H2020-JTI-IMI2-101005122; in part by the AI for Health Imaging Award, CHAIIMELEON, under Grant H2020-SC1-FA-DTS-2019-1 952172; in part by the Medical Research Council under Grant MC/PC/21013; and in part by the U.K. Research and Innovation Future Leaders Fellowship under Grant MR/V023799/1.  
(Corresponding author: Guang Yang.)

**Yutong Chen** is with the National Heart and Lung Institute, Imperial College London, London SW3 6NP, U.K., with the Cardiovascular Research Centre, Royal Brompton Hospital, London SW3 6NP, U.K., and also with the Faculty of Biology, University of Cambridge, Cambridge CB2 1RX, U.K.

**Carola-Bibiane Schönlieb** is with the Department of Applied Mathematics and Theoretical Physics, University of Cambridge, Cambridge CB3 0WA, U.K.

**Pietro Liò** is with the Department of Computer Science and Technology, University of Cambridge, Cambridge CB3 0FD, U.K.

**Tim Leiner** is with the Utrecht University Medical Centre, 3584 CX Utrecht, The Netherlands.

**Pier Luigi Dragotti** is with the Department of Electrical and Electronic Engineering, Imperial College London, London SW7 2BU, U.K.

**Ge Wang** is with the Biomedical Imaging Center, Rensselaer Polytechnic Institute, Troy, NY 12180 USA.

**Daniel Rueckert** is with the Department of Computing, Imperial College London, London SW7 2BU, U.K., and also with the Institute for Medical Informatics, Statistics and Epidemiology, Technical University of Munich, 81675 Munich, Germany.

**David Firmin** and **Guang Yang** are with the National Heart and Lung Institute, Imperial College London, London SW3 6NP, U.K., and also with the Cardiovascular Research Centre, Royal Brompton Hospital, London SW3 6NP, U.K. (e-mail: g.yang@imperial.ac.uk).

This article has supplementary downloadable material available at <https://doi.org/10.1109/JPROC.2022.3141367>, provided by the authors.

---

Digital Object Identifier 10.1109/JPROC.2022.3141367

are then inferred from the existing k-space points. This leads to an acceleration that is inversely proportional to the undersampling ratio. For example, if only 50% of the k-space is sampled, the acceleration is twofold (excluding scanning preparation and/or prescanning time). Among different undersampling techniques [1], compressed sensing (CS) yields an aggressive acceleration rate up to 12.5-fold [5]. CS assumes that, if the undersampled signals can be compressed accurately, they can be decompressed or reconstructed accurately [2], [6] without the need for full sampling. Thus, CS extrapolates unknown k-space signals from existing ones, akin to image super-resolution techniques that increase image resolution by reconstructing high-frequency image details [7].

Driven by the growing research on deep learning in computer vision, deep-learning-based algorithms have gained popularity for CS-based MRI (CS-MRI) reconstruction. Deep learning techniques utilize artificial neural networks (ANNs) to learn the CS reconstruction process. Compared with traditional nondeep-learning-based approaches, deep learning enables higher quality reconstruction [3], [8]–[10] and the acceleration ratio of MRI acquisition. With an exponentially increasing interest toward deep-learning-based CS-MRI, the complexity and diversity of the reconstruction algorithms have increased dramatically. Motivated by this rapidly expanding field, we have conducted a systematic review and the first meta-analysis to summarize the development of deep-learning-based CS-MRI. We will outline the background of deep learning in CS-MRI reconstruction, review each algorithmic category, present the results of meta-analysis, and conclude with an outlook on deep-learning-based CS-MRI acceleration.

## A. Deep Learning

The power of deep learning centers on its capacity to model complex input–output relationships with a large number of parameters in an ANN [11]. An ANN consists of an input layer of nodes, followed by multiple hidden layers and an output layer (see Fig. 1 in the Supplementary Material). In CS-MRI, each input node represents a pixel in the undersampled MR image. The pixels are weighted and summed to form the input for the next layer after a nonlinear activation function [12]. The subsequent hidden layers perform a similar process to produce the final reconstructed image.

The connection weights are network parameters that are optimized such that the outputs from the network are as similar to the target outputs as possible. That is, the network weights need to be tuned to minimize the difference between the fully sampled images and the reconstructed images. This process of weight optimization is known as training the ANN. The training process is guided by the difference or error between actual and desired outcomes, described by a loss function. In other words, the network receives the undersampled images and

outputs the reconstructed versions. The loss function computes the discrepancy between actual and desired outputs, and utilizes this information to update the parameters of the ANN that models an optimal CS-MRI reconstruction process.

## B. End-to-End

Deep-learning-based CS-MRI models fall into two main categories: end-to-end (ETE) and unrolled optimization (UO) [13]–[15]. An ETE technique models the CS-MRI reconstruction process directly. In CS-MRI, the process of acquiring undersampled images is

$$y = UFx \quad (1)$$

where  $x$  is the fully sampled image,  $Fx$  is the Fourier transform of the image, i.e., its k-space representation,  $U$  is a binary matrix of zeros and ones that denote which k-space locations to the sample, and  $y$  is the undersampled k-space data [2]. ETE techniques model the inverse acquisition or reconstruction process directly, mapping from  $y$  to  $x$ , and, hence, the name “ETE.” Because of this direct mapping, the reconstruction process is usually fast [14].

An advantage of ETE models is that advances from other fields of deep learning are transferable to ETE designs (see Table 1 in the Supplementary Material). For example, U-Net [16], a deep learning model originally developed for image segmentation was readily applied to reconstruct MR images in an ETE manner without major modifications [3], [17]. Similarly, a self-attention mechanism—designed to enhance natural image processing—was incorporated into deep ETE models with performance improvement over U-Net [18]. One limitation is that ETE models tend to require a larger sample size to train [13].

## C. Unrolled Optimization

UO combines deep learning with traditional iterative CS algorithms. Traditional CS techniques solve the general problem of image recovery

$$\frac{1}{2} \|UFx - y\|_2^2 + R(x) \quad (2)$$

in which  $x$  is the reconstructed image and the first term enforces the data fidelity, i.e., the reconstructed image does not differ from the undersampled one at the sampled k-space locations. The second term imposes regularization, typically sparsity constraints, on the reconstructed image to satisfy the CS criteria. Deep learning networks form the regularizer term (see Table 1 for example). That is, deep learning models are designed to learn the regularization methods to constrain image reconstruction, rather than directly modeling the reconstruction process itself. From a Bayesian perspective, the regularizer term represents the prior knowledge about the property of the reconstructed

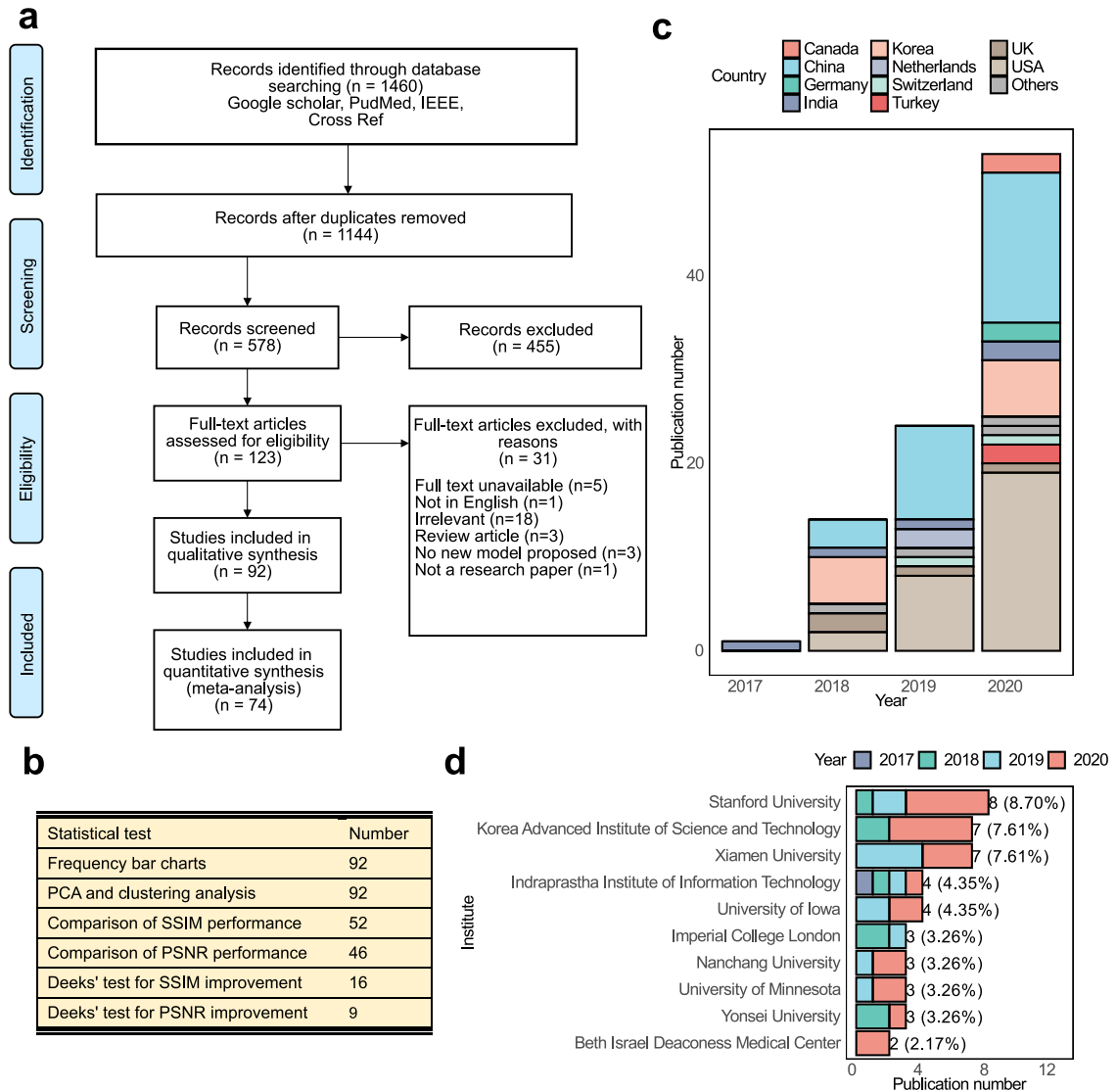


**Fig. 1.** Basic information of the reviewed studies. (a) Preferred reporting items for systematic reviews and meta-analyses (PRISMA) [109] flow diagram of this meta-analysis study. (b) Number of studies used in each analysis test. Abbreviations: PCA: principal component analysis; SSIM: structural similarity index, a popular metric of performance of deep learning model in CS reconstruction; and PSNR: peak signal-to-noise ratio. (c) Number of publications in each country over time. (d) Number of publications by the research institute. The number in the bracket indicates the proportion of the publications from the institute among all the studies that met the inclusion criteria (see Section IV-A).

image [19], e.g., sparsity (see Section II-A in the Supplementary Material). Therefore, compared with ETE techniques, UO incorporates prior domain knowledge about the expected property of MR images [15]. This reduces the solution space and facilitates model convergence and performance [13]. It may underpin the superior performance of UO methods compared with ETE ones [15] with fewer parameters [14].

Furthermore, different networks with different weights or parameters can be used in different iterations of UO. In each iteration, each subnetwork has a relatively small

receptive field and can perform the local transformation. This can avoid overfitting as may occur in ETE models [10]. Compared with using the same network with the same weights in each iteration, this no-weight sharing approach has demonstrated superior performance [9], [20], [21] with some exceptions [22]. Building upon this no-weight sharing approach, Zeng *et al.* [23] incorporated dense connections between subnetworks, a technique inspired by image super-resolution literature. This allows each subnetwork to receive the output from all the preceding subnetworks [23]. These developments

**Table 1** Summary of the Regularizer Terms Used in Deep UO and Their Relationship to the Corresponding Traditional CS Techniques

Traditional	Deep-learning-based	Regularizer	References
DL <sup>a</sup>	Deep DL	$\ z\ _1$	[24], [25]
pFISTA-SENSE <sup>b</sup>	pFISTA-SENSE-Net	$\ \Psi x\ _1$	[26]
TV <sup>c</sup>	TVINet	$\ \nabla x\ _1$	[27]
IFR-CS <sup>d</sup>	IFR-Net	$\sum_i \lambda_i \ k_i x\ $	[20]
SLR <sup>e</sup>	H-DSLR	$\ \mathcal{T}(\mathcal{F}\nabla x)\ _*$ <sup>f</sup>	[28]
SToRM <sup>g</sup>	MODL + SToRM	$\ R(x)\ ^2 + \text{Tr}(x^T L x)$	[29]
fields-of-experts <sup>h</sup>	VN	$\sum_i f_i(k_i x)$	[30]

<sup>a</sup>**DL:** Dictionary learning. Here  $z$  is the latent dictionary representation or transformation of the input image. The regularizer term enforces sparsity on this dictionary representation to satisfy CS criteria. In deep dictionary learning, multiple layers of dictionaries learn this latent transform  $z$ .

<sup>b</sup>**pFIST-SENSE:** Projected fast iterative soft-thresholding algorithm-sensitivity encoding. It uses a transform  $\Psi$  to enforce sparsity of the reconstructed image  $x$ . In the deep-learning version, this transform is replaced with a neural network.

<sup>c</sup>**TV:** Total variation. It enforces smoothness on the reconstructed image by minimizing changes in the gradient of the image. In the deep-learning version, the gradient operator  $\nabla$  is replaced with a neural network.

<sup>d</sup>**IFR-CS:** Iterative feature refinement-compressed sensing. The regularizer applies convolutional filters  $k_i$  to the reconstructed image.

<sup>e</sup>**SLR:** Sparse and low rank approach. The regularizer minimizes the nuclear norm, i.e., the rank of the Hankel matrix  $\mathcal{T}$ . In the deep-learning version, this operation is replaced with a neural network.

<sup>f</sup>The \* subscript means the nuclear norm.

<sup>g</sup>**SToRM:** Smoothness regularization on manifolds. The regularizer has a general form  $R(x)$  which can be replaced with a neural network. The second term is a SToRM prior, which uses a Laplacian manifold  $L$  to exploit similarity beyond local neighbor.

<sup>h</sup>**Fields-of-experts:** Convolutional kernels  $k_i$  operate on the reconstructed image  $x$ , followed by trainable activation functions  $f_i$ .

show that UO is a robust, flexible, and powerful deep-learning-based CS-MRI technique.

Compared with ETE models, the iterative nature of UO increases the computation time. This arises from the need to update both the network weights and the reconstructed images to maintain k-space data fidelity [see (2)]. In contrast, ETE methods only need to optimize and update network parameters during the training procedure. To mitigate the iterative nature of updating the reconstructed image, one approach trains the deep-learning-based regularizer term alone without the data fidelity term [31]–[34] in (2). Then, during image reconstruction, the trained regularizer is reincorporated to optimize the reconstructed image. This solution decomposes the process of optimizing the network parameters and images into optimizing them separately.

The second, and more popular approach, is to train the unrolled model in an ETE fashion by expressing (2) in a close form. To illustrate, the deep cascaded convolutional neural network (DC-CNN) [10] applies the following loss

function to update the network parameters and reconstructed images:

$$\underset{x, \theta}{\operatorname{argmin}} \|U F x - y\|_2^2 + \lambda \|x - f(x|\theta)\| \quad (3)$$

where  $\theta$  denotes all network parameters,  $f(x|\theta)$  denotes the output of the deep learning regularizer, and  $\lambda$  is a scalar to adjust the relative contributions of the two terms. The closed form of (3) is

$$x = \frac{\lambda y + F f(x|\theta)}{\lambda + 1}$$

at k-space locations that are sampled and

$$x = f(x|\theta)$$

at k-space locations that are not sampled.

We can also interpret this closed form as another computation layer, called the *data consistency* layer, in deep learning models. The process of iteratively reconstructing

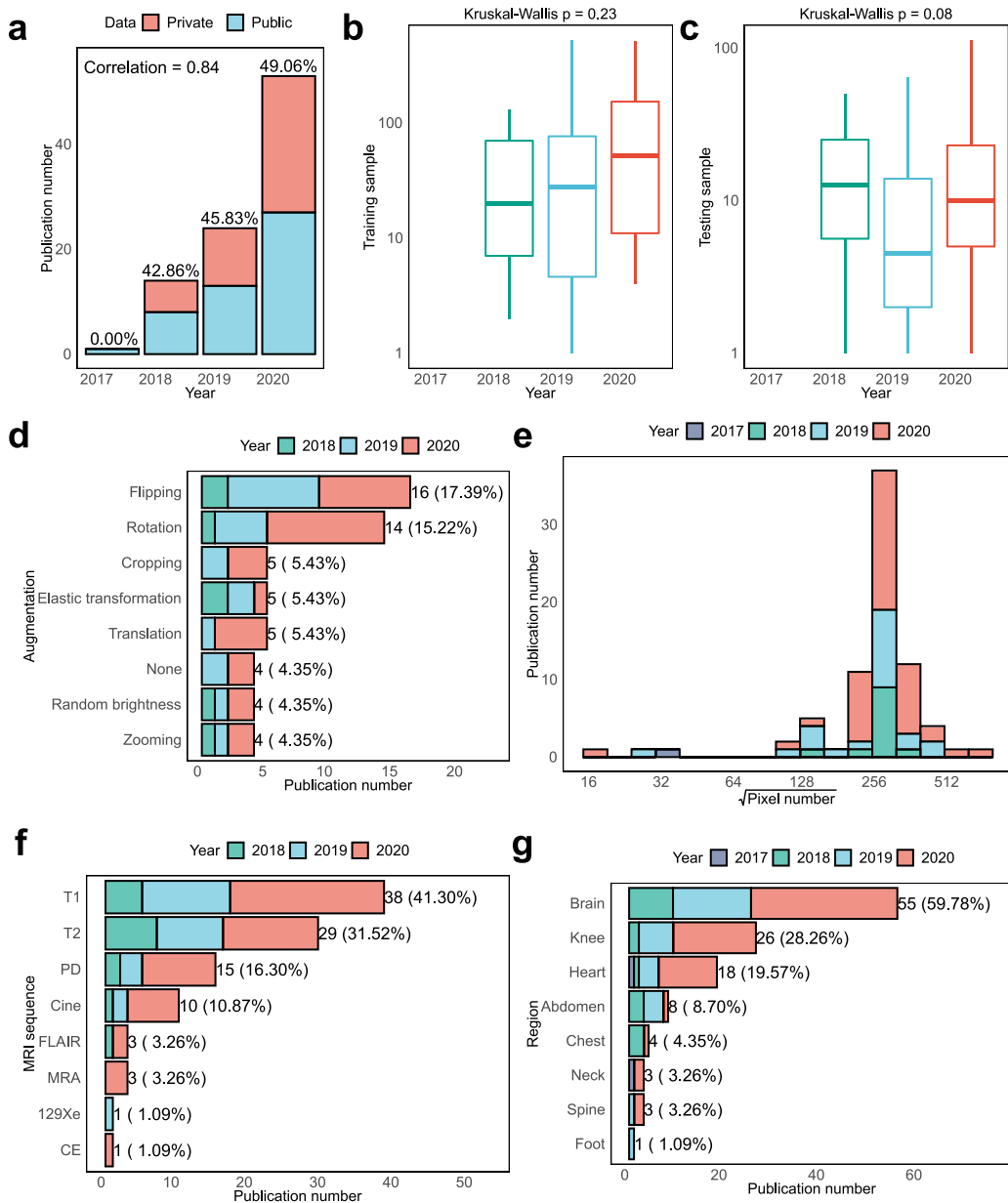


**Fig. 2.** Features of the datasets used by different studies. (a) Number of publications that use public and private datasets over time. The proportions of studies using public datasets are labeled above each bar. The correlation of these proportions with publication time was 0.839 (top left corner). Boxplot showing training (b) and (c) testing sample sizes over time. The p-value of changes over time from the Kruskal-Wallis test is shown above each plot. (d) Histogram of the square root of pixel number of the input image to the deep learning models. For example, “256” indicates that the input image is  $256 \times 256$  in size. (e) MRI sequence of the images in the datasets used by different studies. Abbreviations: PD: proton density (including those with and without fat suppression); MRA: magnetic resonance angiography; 129Xe:  $^{129}\text{Xe}$  imaging; and CE: contrast enhanced. (f) Anatomical region of the images in the datasets used by different studies. (g) Data augmentation techniques used by different studies.

the MR images and updating model parameters is a cascade of alternating model reconstruction and data consistency reinforcement (see Fig. 2 in the Supplementary Material). In other words, this cascade of neural networks becomes an ETE model and is trained in the same fashion. DC-CNN has, since then, become an integral part of subsequent model designs [8], [9], [34], [35], [36, p. 2], [37]–[40]. However, DC-CNN is not computationally

efficient for parallel imaging-based CS acquisition [41], potentially preventing the wider spread of DC-CNN-based methods. Moreover, one cannot always derive the closed form of other loss functions as trivially as in DC-CNN [42]. To circumvent this problem, some models apply simple gradient descent [30], [43]–[45], conjugate gradient descent [22], [29], [46], or auxiliary variables [21] (see Sections II-B-II-D in the Supplementary Material) to

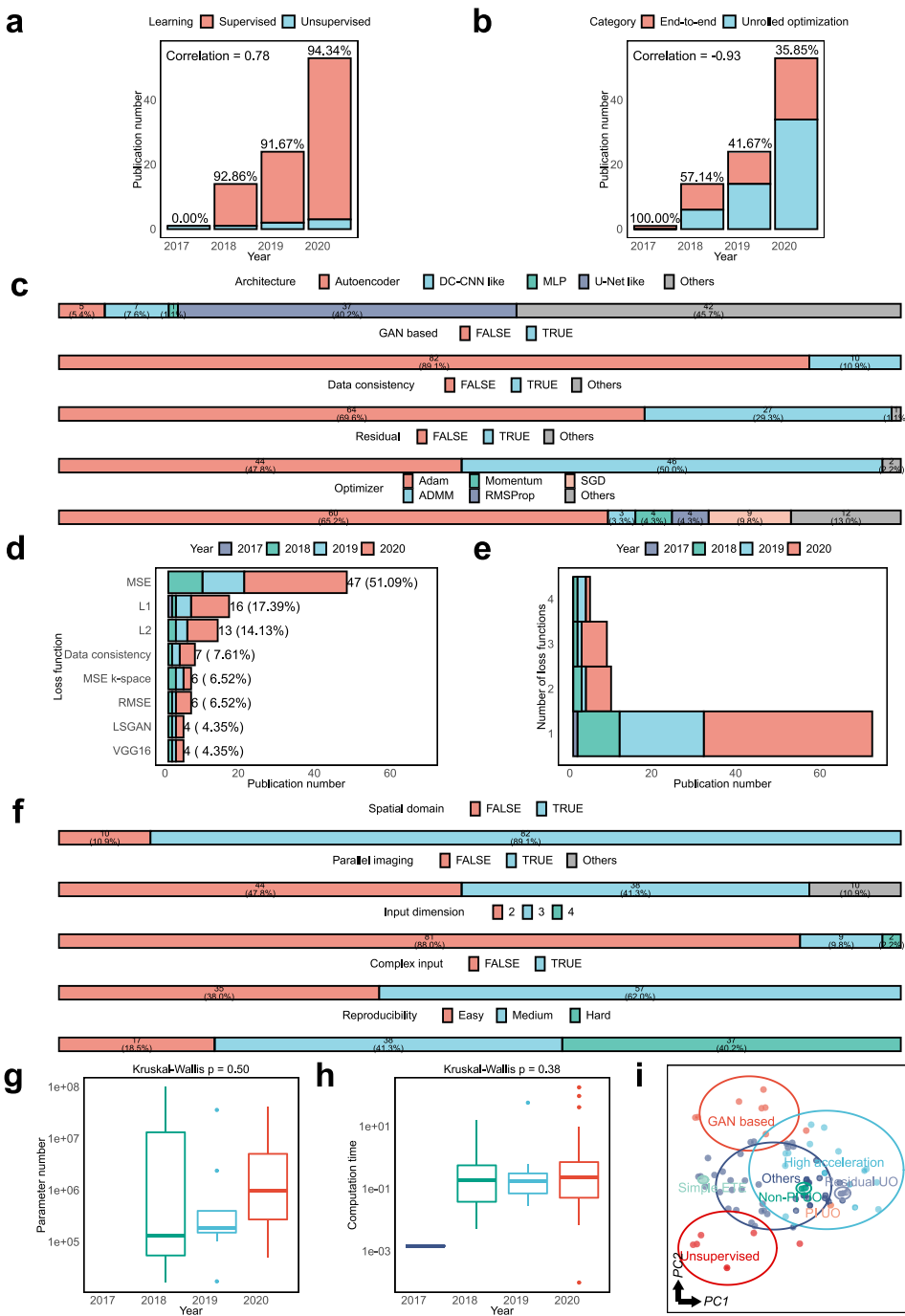


**Fig. 3.** Neural network design traits. (a) Number of publications over time by whether the model applies supervised learning. The proportion of unsupervised learning studies is in the text above each bar. (b) Number of publications over time by model category. The proportion of ETE models is indicated in the text above each bar. (c) Number and proportion (in square brackets) of studies that use each of the key design traits in deep learning models. The field “others” indicate the studies that did not report the relevant design traits. (d) Loss functions used by different studies. Abbreviations: MSE: mean square error between the reconstructed image and ground truth; L1: L1 loss function; L2: L2 loss function; data consistency: difference between the reconstructed image and ground truth at undersampled k-space pixels; RMSE: root mean square error; LSGAN: least-squares generative adversarial network; and VGG16: difference in the image embedding from the VGG16 network between the reconstructed image and ground truth. (e) Number of loss functions used by different studies. (f) Input image characteristics. (g) Computation time over time. (h) Number of parameters over time. The p-value at the top was calculated using the Kruskal-Wallis test. (i) PCA of all the models. Each dot represents one model. The dots are colored according to the GMM cluster they belong to. The position and size of the ellipses represent the mean and twice the standard deviation of each Gaussian model in the mixture, which is projected onto PC1 and PC2. Abbreviations: simple ETE: simple end-to-end models; PI UO: parallel imaging-based unrolled optimization; non-PI UO: unrolled optimization without implementing parallel imaging; and residual UO: unrolled optimization that implements residual learning.

implement UO in an ETE fashion to facilitate the model training process.

While unrolled methods can be trained ETE, ETE methods can incorporate features of UO. For example, various ETE models integrate the data consistency layer to enforce k-space data consistency [47]–[51]. It enables ETE methods to enjoy the benefits of enforcing data fidelity. Therefore, combining ETE and unrolled features in a single model may increase the diversity of network designs that also share the benefits of both categories.

#### D. Unsupervised Learning

The above discussion on unrolled versus ETE models assumes that the ground-truth MR images are available to train the model to learn the mapping between the undersampled images and the ground truth. That is, the training process is supervised. If the ground-truth images are not available, the model requires unsupervised training [52]. The objective is to minimize the difference between reconstructed images and the undersampled images at the undersampled k-space locations, i.e., enforcing data consistency [52]. Even without fully sampled ground truth, unsupervised models can remove undersampling artifacts effectively. The reason is that, even without training, a deep learning model can capture a great deal of image statistics [53]. Most unsupervised methods use UO and alternately optimize the reconstructed images and the model parameters [24], [25], [54], [55]. Only one study implements an ETE training [52]. Most studies demonstrate higher quality reconstruction over traditional CS techniques [24], [25], [54], [55] and the supervised learning model [21], ADMM-CSNet [24]. This underscores the prospect of unsupervised learning when ground-truth images are unavailable.

## II. NETWORK ARCHITECTURES

Having surveyed the two main categories of deep-learning-based CS-MRI techniques, we will visit the key milestones during the development of deep-learning-based CS-MRI (see Fig. 3 in the Supplementary Material) (for less commonly used designs, refer to Section I in the Supplementary Material).

#### A. Variational Network

A variational network (VN), an UO method, uses field-of-expert function as a regularizer in the image reconstruction loss function [30], [43]–[45] [see (2)]. Field-of-experts apply convolutional filters on the input undersampled images followed by activation functions. Unlike the activation functions used in typical neural networks, these functions are trainable. The trainable convolutional filters and activation functions are optimized to perform image regularization (see Table 2 in the Supplementary Material). The strength of VN is that they require 10 to 100 times fewer parameters than a typical deep-learning-based CS-MRI model. Therefore, the

computational load may be lower with a smaller risk of overfitting. This has a greater potential for the more computationally demanding 3-D or 4-D reconstruction [45].

#### B. Generative Adversarial Network

The generative adversarial network (GAN) has revolutionized the field of synthesizing photorealistic images [50], [56]. A GAN consists of a generator and a discriminator. The discriminator has trained to label the ground-truth MR images as being “real” and the reconstructed MR images as “fake.” The generator does the opposite: its reconstructed images resemble fully sampled ones such that the discriminator would label the reconstructed images as “real.” With an optimal discriminator, the generator minimizes the Shannon-Jensen divergence between the reconstructed and fully sampled images (see Section II-E in the Supplementary Material). The dealiasing GAN (DAGAN) [3] pioneers GAN-based CS-MRI, which consists of 10.8% of the models in this review [48], [50], [57]–[63]. DAGAN has achieved superior reconstruction performance compared with traditional CS techniques and ADMM-Net [64].

However, GAN suffers from training instability, slow convergence to the global minimum [65], [66], and vanishing gradient [67]. The Wasserstein GAN (WGAN) could mitigate these issues [68]. Instead of the Shannon-Jensen divergence, WGAN minimizes the Wasserstein distance between the reconstructed and fully sampled images. WGAN-based models outperform DAGAN and cycle-GAN [59], [61], which do not use WGAN. Another limitation of GAN is that they “overemphasize the high-frequency texture, thus, ignore image contents [50], and can produce oversmoothed appearance [69].” The least-squares GAN (LSGAN) can address this problem [48], [62]. Taken together, while WGAN addresses the training instability of GAN, LSGAN may tackle the high-frequency texture issue.

Our interpretation of the effectiveness of GAN-based methods may be confounded by other model design elements. For example, in all GAN-based methods, the loss functions also penalize the deviations between reconstructed and fully sampled images in the image and/or k-space domain. Some studies penalize the perceptual quality difference using the VGG16 network [3], [59]; others enforce k-space data fidelity [57]. Nevertheless, without other penalty terms, a GAN-only model still outperforms ADMM-Net [3]. Therefore, GAN-based techniques are promising CS-MRI reconstruction methods, whose performance can be further enhanced by auxiliary penalties.

#### C. Input Domain

Among the studies in this review, 89.1% of the proposed models reconstruct the undersampled input in the image domain. Three studies [70]–[72] operate on the undersampled k-space with higher reconstruction accuracy compared with the image-domain techniques, e.g., DC-CNN

**Table 2** Modified CLAIM Criteria for Collecting Information From Each Paper During the Meta-Analysis

Category	CLAIM number <sup>a</sup>	Item	Explanation
Data	7, 10	Dataset	What the dataset(s) was, how it was collected, selection of subsets if appropriate
		Region	Which region(s) of the body the images in the dataset covered
		MRI sequence	What the MRI sequence was, e.g., T1, T2 etc
	14	Ground truth	What the ground truth was and how it was generated
	20	Partition	How the dataset was partitioned into training, validation, and testing subsets in terms of number of images, patients or MR scans
	25	Augmentation	How the training dataset was augmented
Model	34	Clinical feature	Whether the dataset contains images of pathology
	22	Category	What category the model belonged to, i.e., unrolled optimization, end-to-end, or reference-driven
	22	Architecture	What the structure of the model was, e.g., U-Net, DC-CNN like etc
		Channel number	How many coils the inputs signals to the model were
		Channel merging	If the method uses multicoil input, i.e., a parallel imaging method, how the multicoil data was merged to produce a single final reconstructed image
	22	Input domain	Whether the model was designed to process raw k-space data, magnitude or complex image space data
	22	Dimension	What image dimension the model was designed to process, e.g., 2D spatial, 3D spatial, or 2D spatial-temporal
		Input size	What size of the input MR images was, e.g., 256 x 256
	22	Loss	Which loss function(s) were used to train the model
	22	Optimizer	Which optimizer was used to update and optimise network parameters, e.g., Adam, RMSProp
Evaluation method	23	Open source	Whether the link to the source code is mentioned in the main paper or supplementary file
	23	Platform	Which deep-learning library was used to build the model, e.g., tensorflow, pytorch
		Mask	What pattern(s) of undersampling mask was used, e.g., radial, variable density
		Acceleration	Under which acceleration ratio(s) the model reconstructed the undersampled images
		Comparison	What other algorithms were used to compare the performance of the proposed algorithm

**Table 2** (Continued.) Modified CLAIM Criteria for Collecting Information From Each Paper During the Meta-Analysis

	Metric	What quantitative and qualitative metrics were used to evaluate reconstruction accuracy, e.g., NMSE, PSNR and SSIM
5	Testing mode	Whether the model was tested prospectively (acquire the undersampled image via compressed sensing), retrospectively (undersampled after standard full acquisition or an established compressed sensing approach) or both
Result	36 Result	What were the quantitative data of performance metrics and/or qualitative comparison of representative reconstructed images
	Computation time	Computation time in seconds on a GPU per reconstructed image
Discussion	Novelty	What aspects of the model were novel, i.e., not previously reported
	Strength	What problem in particular the model was designed to address
38	Limitation	What problem remained in the model

<sup>a</sup>The CLAIM item numbers that our proposed review criteria correspond to.

and VN [71]. Two studies [32] and [73] use a hybrid of k-space and image space. That is, for a 2-D undersampled k-space input, inverse Fourier transform was performed along the  $x$ -axis. This means that the  $x$ -axis represents the image-domain information and the  $y$ -axis k-space signals. The performance is higher over the image-domain method, ADMM-Net [73].

The cross-domain design, an increasingly popular strategy, leverages signals from multiple domains. KIKI-net pioneers cross-domain networks [8]. It concatenates a subnetwork operating on the k-space (k-net) with another subnetwork on the image domain (i-net) and so on. The undersampled k-space signals are first reconstructed by the k-net, followed by the inverse Fourier transform to the image domain to be processed by the i-net (see Fig. 2 in the Supplementary Material). A similar network design follows [63] and [74]–[76]. Apart from k-net and i-net, one study [40] concatenates a w-net, a subnetwork that operates on the wavelet domain of the input image. The advantage of a cross-domain network is that the k-space-based network excels in removing high-frequency artifacts. The image-space network improves image sharpness and clarity [8]. The wavelet-domain network exploits both spatial and frequency features that may potentially accelerate feature learning [77]. Consequently, cross-domain networks outperform networks that operate only in the image domain [40], [63], [76], [78].

Besides joining subnetworks on different domains in series, some cross-domain networks concatenate subnetworks in parallel (see Fig. 2 in the Supplementary Material) [38], [79]. The undersampled k-space signals are supplied to a k-net. In parallel, the undersampled image from the inverse Fourier transform is supplied to an i-net. Extensive connections between k-net and i-net facilitate

the learning of a noise-free latent representation of the input image. This design surpasses image-domain methods in reconstruction quality, including ADMM-CSNet (both studies), DC-CNN [79], and DAGAN [38]. However, cross-domain models are limited by their increased parameter numbers. To satisfy hardware requirements, each subnetwork in the IKIK-net needs to be trained separately [8]. This imposes challenges for training cross-domain models despite their exciting prospect by correcting undersampling artifacts from multiple domains [40].

## D. Residual Learning

Residual learning (in 51.1% of deep-learning-based CS-MRI designs) learns the difference or the residual between the ground truth and undersampled input, outperforming nonresidual learning [3], [9]. The rationale is to “constrain the generator to reconstruct only the missing details and prevent it from generating arbitrary features that may not be present in real MR images” [3]. Residual learning can also mitigate training difficulty as the topological complexity of the residual difference may be smaller compared to the entire MR image [47]. This effectiveness has been justified by the persistent homology analysis [17].

## E. Attention

An attention module is a computational layer in the neural network [51], [81]. This module learns the most important pixel in the input to attend to, i.e., learning the optimal weights assigned to each pixel. Compared with the same model without attention modules, this design achieves a higher reconstruction accuracy. However, a key limitation of attention modules is their high computational demand, which is addressed by the memory-efficient self-attention module proposed by Zhou *et al.* [82].

### III. IMAGE REDUNDANCY

Another important technique to accelerate AI-powered fast MRI is image redundancy. Between 2019 and 2020, there has been a trend toward exploiting MR image redundancy across multiple contrasts, spatiotemporal dimensions, and parallel imaging coils to improve performance and acceleration rates.

#### A. Redundancy Across Contrast Modalities

Different clinical settings demand different contrasts for MR images, e.g., T1 weighted, T2 weighted, and proton density. For example, T1 weighted images provide detailed anatomical structures, while pathological features are usually more apparent in T2 weighted images [4]. To improve the clinical diagnostic power, MR images of multiple contrasts are required [83]. Because images with different contrasts of the same structure convey similar anatomical information, the information redundancy can be used to accelerate CS-MRI.

Among the reviewed studies, the earliest [84] uses fully sampled T1 weighted images to guide the reconstruction of the corresponding undersampled T2 weighted images. T1 weighted and T2 weighted images are concatenated as a two-channel input to the deep learning model. This method achieves superior reconstruction performance compared with the model without the fully sampled T1 weighted image. A similar design was employed in [48]. Other studies [44], [85] concatenate undersampled images without the guidance of fully sampled ones. Alternatively, two separate networks are trained for separate contrasts with extensive crosstalk between the two networks, outperforming the same network without multicontrast information [86]. However, the limitation of multicontrast reconstruction is that signals from one contrast may leak into another [44]. Furthermore, the network cannot process an arbitrary number of contrasts without significant structural modifications. Despite these shortcomings, multicontrast MR reconstruction represents a significant step forward in exploiting MR image redundancy.

#### B. Spatiotemporal Redundancy

Spatiotemporal redundancy increases in higher dimensional MR images. To illustrate, in 3-D imaging, structures in two neighboring planes are unlikely to be drastically different and are correlated. Likewise, in 4-D imaging (3-D spatial plus a temporal dimension), the structures between two adjacent time frames are correlated. However, extending 2-D deep-learning-based CS-MRI models to 3-D and 4-D usually requires computationally costly 3-D or 4-D convolution operations [87]. To mitigate the 3-D computational demand, most studies [29], [78], [88]–[90] use 2+1 convolution. This involves a 2-D convolution along two dimensions of the input image followed by a 1-D convolution along the rest of the one axis [91]. However, it is difficult to evaluate the performance of 3-D deep-learning-based CS-MRI models against

typical deep learning methods, most of which (88.0% of the reviewed studies) target 2-D reconstructions. Despite the computational challenge and the lack of evaluation frameworks, two studies [45], [92] venture into 4-D MRI reconstruction. Analogous to 2+1 convolution, 3-D spatial convolution followed by 1-D temporal convolution is applied [92]. Hence, multidimensional MR image reconstruction tends to avoid computationally costly multidimensional convolutions.

#### C. Parallel Imaging With Coil Redundancy

In 41.3% of the reviewed studies, parallel imaging is combined with CS to exploit the k-space signal redundancy collected by multiple receiver coils. Similar to multicontrast reconstruction, for separate imaging coils, many studies use separate input and outputs channels [17], [40], [57], [70], [75], [76], [78], [80], [93]–[95]. The reconstructed images for each coil are then combined by the sum-of-squares. One exception [94] uses a separate network to perform the coil combination. However, neither design can handle signals of an arbitrary number of coils.

Another approach is to incorporate parallel imaging into the optimization objective. To illustrate, the coil sensitivity matrix  $S_i$  describes the regions that a particular coil  $i$  is most sensitive to. Then, the image acquisition model (1) and the training objective (2) can be modified, respectively, as

$$y_i = US_i Fx$$

and

$$\frac{1}{2} \|US_i Fx - y\|_2^2 + R(x).$$

Deep learning models can be modified accordingly [12], [20], [26], [30], [43]–[45], [78], [92], [93], [96]–[101].

While deep parallel imaging CS techniques can further accelerate MR acquisition, evaluating their performance against single-coil reconstructions is challenging. This is because different datasets are required for multi- and single-coil applications. Alternately, coil compression of raw undersampled multicoil data into a single coil may be used, but this comparison may not be fair [102]. Furthermore, in various multicoil studies, coil compression of the multicoil raw data into a smaller number of virtual coils was applied [41], [45], [90] to reduce the computational demands. It is unclear whether this measure can best utilize the multicoil information or reflect the model performance on raw uncompressed multicoil signals. Despite various computational and evaluational challenges to exploiting multicontrast, spatiotemporal, and parallel imaging redundancies, the recent developments reflect the remarkable community efforts in improving the speed and accuracy of CS-MRI.

## IV. META-ANALYSIS METHOD

### A. Data Collection

To quantitatively evaluate the trend of deep-learning-based CS-MRI development, we mined the literature across four platforms: Google Scholar, PubMed, IEEE, and Crossref. We used the keyword: “MRI,” “reconstruction,” and “deep learning.” The key word “compressed sensing” was not incorporated to broaden the search range. The search was carried out on October 22, 2020. The Publish or Perish software was used to search through Google Scholar, PubMed, and Crossref. Xplorer was used for IEEE journals. The references of the matched studies were exported as a .ris file and imported into Mendeley Desktop. Using the “Update Details” function in Mendeley Desktop, the details of all the references were updated automatically. To facilitate subsequent filtering statistical analysis, the references were transferred to Zotero, which enables the export of the references as a.csv file. For consistency, Zotero was the reference manager for this article.

**1) Initial Filtering:** Initially, 1460 studies were identified that matched the three search keywords. Then, 301 duplicates were removed based on a case-insensitive match of the titles of the papers, leading to 1159 nonduplicated studies. Then, the studies without titles or authors were removed, leaving 1144 studies for subsequent analysis. We excluded preprints, conference papers, and other items that are not published in research journals for this review. This was done via a case insensitive search for the following keywords in the journal names and publishers of the papers: “arxiv,” “spie,” “mirasmart,” “proceeding,” “patent,” “openreview,” “aaai,” “conference,” “book,” “preprint,” “meeting,” “symposium,” “workshop,” “ismrm,” “Proc Intl Soc Mag Recon Med,” “icassp,” “nips,” “lectures,” “book-chapter,” “proceedings-article,” “posted-content,” “monograph,” and “dissertation.”

After filtering, 578 studies remain for a title and abstract screening.

**2) Title Screening:** Two independent reviewers determined the relevance of a research paper by screening its title. Our title screening criteria are that a study was removed if its title contains fewer than two of these three keywords: “CS,” “MRI,” and “deep learning.” Any discrepancy between the two reviewers was resolved by the opinion of the more senior reviewer. After title screening, 221 studies entered the abstract screening stage.

**3) Abstract Screening:** One reviewer performed abstract screening. The criterion was whether the abstract mentions all three of the keywords: “CS,” “MRI,” and “deep learning.” If an abstract was generic, the introduction of this article was briefly examined. Only 123 studies passed our abstract screening criteria.

**4) Full-Text Screening:** Only studies with full text available in English and that proposed a new deep learning model for CS-MRI were included. The full text was screened by one reviewer, and the results were scrutinized

by a more senior reviewer. In the final review process, 92 studies were included. The entire process of literature screening and exclusion is summarized in Fig. 1(a).

**5) Data Collection:** To summarize the key model design traits, criteria in the Checklist for Artificial Intelligence in Medical Imaging [103] were modified and tailored for deep CS-MRI studies (see Table 2). For example, the modified checklist incorporated items that are salient for CS experiments but not necessarily for general-purpose imaging analysis. This includes the pattern of undersampling mask, acceleration ratio tested in the study, types of performance metrics, and so on. All data were collected by one reviewer and verified by another reviewer. Quantitative performance measures data were collected from the tables in the main text and the Supplementary Material. Initial data cleaning was performed by the text editor vim and later using the programming language R.

### B. Data Analysis

**1) Developmental Trend:** To determine changes in the popularity of deep CS-MRI model design traits, the Pearson correlation was computed between the proportion of models using a particular trait and the year of publication. To assess whether numerical variables, such as training or testing sample sizes, change over time, the *p*-value was calculated. This was achieved by using the Kruskal-Wallis test implemented in the kruskal.test function from R package stats [104].

To evaluate the input image size, the pixel number of the input images to the models was calculated as followed. If more than one size were reported, the size of the image that was mentioned first in this article was chosen. Then, the width and the height of the image were multiplied to obtain the pixel number. For studies that process 3-D or 4-D images, the dimensions along the *x*- and *y*-axes are chosen instead.

To evaluate the reproducibility of different studies, the scoring was based on a previous review paper [105]. Studies that publish neither the code nor the dataset are classified as “hard to reproduce.” Those that publish only the code or only the dataset are “medium to reproduce.” Those that release both are “easy to reproduce.”

**2) Clustering:** The following features were used to perform clustering analysis: GAN-based, U-Net-like, mean square error (MSE) loss, supervised, residual, complex input, parallel imaging, maximum acceleration, dimension, data consistency, and spatial domain. Features not reported by most of the studies were excluded. The clustering algorithm was a Gaussian mixture model (GMM), implemented by the Mclust function from the R package mclust [106]. The number of mixture models was chosen to be between 1 and 20. Using Bayesian information criteria, the optimal number of models was determined to be 8. The cluster names were annotated based on the design traits within each cluster.

To visualize the clusters, the principal component analysis (PCA) was performed using the `prcomp` function in the R package `stats`. The means and variances of each Gaussian model cluster along all the features are projected onto the first two principal components and visualized as ellipses. The centers of the ellipses are the projected means. The axes lengths are twice the square root of variances, representing a 95% confidence interval.

The extent to which metrics are linearly correlated was quantified using the  $R^2$  value. This was calculated on the author's reported performance of a model at different acceleration ratios over two chosen metrics. The  $R^2$  value was obtained using the `lm` function in the R package `stats`.

*3) Performance:* To quantify the improvement of a model over zero-filling reconstruction, the model performance at a particular metric was divided by the zero-filling performance to obtain the odds' ratio. If the performance data at more than one acceleration were available, the mean of the odds' ratio was calculated. Deeks' test for publication bias [107] was then carried out by calculating the *p*-value of the regression line between the odds' ratio and one over square root of the effective sample size. In this study, the effective sample size was estimated using the testing sample size. The *p*-value was obtained using the `stat_cor` function in the R package `ggnpubr` [108].

All the meta-analyses were performed using the R version 3.6.3 running on Ubuntu 18.04. We have released the source code (<https://github.com/ayanglab/How-to-Perform-Technical-Systematic-Review-And-Meta-Analysis-Tutorial>) for reproducible and sustainable future studies.

## V. META-ANALYSIS RESULTS

Among the 92 studies that meet our meta-analysis inclusion criteria [see Fig. 1(a) and (b)], the publication number increases exponentially from 2017 to 2020 [see Fig. 1(c)]. Most were from China and the USA, accounting for 63.0% of all studies (31.5% from either country) followed by South Korea (12.0%). The institute with the highest number of publications was Stanford University, followed by the Korea Advanced Institute of Science and Technology and Xiamen University [see Fig. 1(d)]. The rising publications underscore the increasing importance of deep-learning-based CS-MRI.

### A. Dataset Characteristics

Training and evaluating deep-learning-based CS-MRI models require ground-truth MR images. In 84.8% of the studies, fully sampled MR images served as the ground truth. However, in 15.2% of the studies, sampling MR images fully was impossible, for example, in cardiac cine imaging, due to the motion artifacts created by constant heartbeats [41]. Thus, CS-based reconstruction of these nonfully sampled images was treated as ground truth.

Regarding the type of datasets, 41 studies (44.6%) used private datasets exclusively, while 30 (32.6%) exclusively used public datasets; 21 (22.8%) used both public and private datasets. The most popular datasets were

human connectome projects (used by 13.0% of the studies; see Table 3), fastMRI (10.9%) and IXI (10.9%), but the tendency to use public datasets decreased over time [see Fig. 2(a)].

Considering the sample size, the mean number of MR scans for model training was 89.9, and that for testing was 20.8. Neither the training nor testing sample size changed significantly over time [see Fig. 2(b) and (c)]. To increase the number of training samples, some studies applied data augmentation. The most popular augmentation techniques were flipping and rotation [see Fig. 2(d)]. Less popular techniques included adding random noise [87], sharpness, contrast [38], and using images of different acceleration ratios [98]. However, few studies assessed the impact of data augmentation on the performance of deep learning models in CS MRI.

For the source of the datasets, most were collected from human volunteers or patients, except three from rats [24], [25], [47]. Most frequently, the spatial resolution of MR images was  $256 \times 256$  MR [see Fig. 2(e)]. The lowest spatial resolution was  $16 \times 16$  reflecting an image patch-based approach [110]. The highest spatial resolution was  $590 \times 590$  [96]. Regarding the contrast of the MR images, T1 weighted and T2 weighted were the most popular [see Fig. 2(f)]. The least popular were MR angiography (MRA), hyperpolarised  $^{129}\text{Xe}$  imaging (129Xe), and contrast-enhanced (CE) MRI, probably linked to the scarcity of publicly available datasets. Regarding the anatomical regions, the most popular were brain (45.45%) and knee (21.49%) [see Fig. 2(g)], as most of the public datasets (see Table 3) consisted of the brain and/or knee images. Cardiac imaging was the third most popular (14.88%). Many (44.4 %) cardiac MRI-based studies utilized the temporal dimension of cardiac imaging, i.e., changes of cardiac MR images over each cardiac cycle. This included 66.9% of the studies that reconstruct 3-D MR images and 100% of those using 4-D images. Hence, the pursuit of multidimensional MRI reconstruction may fuel the interest toward cardiac MRI.

Concerning the pathological features of the datasets, 26.1% of the studies used pathology-free training and testing sets, while 26.1% of the studies included pathology in both sets. Only ten studies (10.9%) included pathology-free training sets and pathology-containing test sets to evaluate the generalizability of a deep learning model in pathology settings. Three studies demonstrated good generalizability [45], [101], [111].

### B. Design

*1) Model Architecture:* We also summarized the design traits of deep learning models. Supervised learning models and unrolled models were increasingly favored, occupying greater proportions of the studies over time [see Fig. 3(a) and (b)]. Most studies (40.2%) use a U-Net-like network, while 7.6% used a structure similar to DC-CNN [10] [see Fig. 3(c)]. U-Net-like networks became

**Table 3** Datasets Used by Each Study

Public dataset	Sample size	Pathology	Region	Used by
<a href="#">SRI24</a> [112]	24 subjects <sup>a</sup>	No	Brain	[85]
<a href="#">MRBrainS13</a> [113]	20 scans	Yes	Brain	[85]
<a href="#">ADNI</a> [114]	NA <sup>b</sup>	Yes	Brain	[8], [111]
<a href="#">NeoBrainS</a> [115]	NA	NA	Brain	[85]
<a href="#">IXI</a>	600 images	No	Brain	[27], [35], [40], [48], [62], [63], [97], [116]– [118]
<a href="#">fastMRI</a> [119]	8400 scans	NA	Brain, knee	[20], [46], [61], [80], [93], [97], [99], [118], [120]
<a href="#">Brainweb</a> [121]	NA	Yes	Brain	[122]
<a href="#">mridata</a>	247 scans	NA	Knee	[71], [118], [122]
<a href="#">Caglary</a> <a href="#">Campinas</a> [123]	212 scans	NA	Brain	[27], [28], [38], [75]
<a href="#">BRATS</a> [124]	300 scans	Yes	Brain	[47], [48], [117]
<a href="#">Dynamic MRI</a> <a href="#">of speech</a> <a href="#">movements</a>	NA	NA	Brain, neck	[125]
<a href="#">MICCAI</a> [126]	47 scans	No	Brain	[3], [59], [127], [128]
<a href="#">HCP</a> [129]	9835 subjects	Yes	Brain	[12], [17], [28], [61], [71], [72], [80], [111], [118], [130]– [132]
<a href="#">Aggarwal 2020</a> [46]	10 subjects	NA	Brain	[46]
<a href="#">Aggarwal 2019</a> [22]	5 subjects	NA	Brain	[22], [100]
<a href="#">OAI</a>	NA	Yes	Knee	[133]
<a href="#">Hammernik</a> <a href="#">2018</a> [30]	100 subjects	Yes	Knee	[26], [28], [30], [39], [46]
<a href="#">Vishnevskiy</a> <a href="#">2020</a> [45]	18 subjects	Yes	Brain	[45]
<a href="#">MSChallenge</a> [134]	35 subjects	Yes	Brain	[63]
<a href="#">CAP</a> [126]	155 subjects	NA	Heart	[127]
<a href="#">Liu 2020</a> [31]	31 scans	NA	Brain	[31]

**Table 3** (Continued.) Datasets Used by Each Study

<a href="#">Sawyer 2013 [135]</a>	20 scans	No	Knee	[47], [98]
<a href="#">MSSEG [136]</a>	53 scans	Yes	Brain	[84]
<a href="#">MRI MS DB</a>	100 subjects	Yes	Brain	[137]
<a href="#">MIDAS [138]</a>	58 subjects	No	Brain	[36], [48]
<a href="#">Liu 2019 [20]</a>	105 images	No	Brain	[20]

<sup>a</sup> For the sample size, we report the size of the combined total datasets if more than one dataset are included on the website.

<sup>b</sup> Information not available from the website of the dataset.

increasingly popular over time (correlation = 0.87; see Table 3 and Section IV-B in the Supplementary Material), while autoencoder-based networks were less popular (correlation = -0.84). GAN-based models, the data consistency layer, and residual learning [10] were used in a considerable proportion of the studies. Both the data consistency layer and residual learning were increasingly incorporated (correlation = 0.91 and 0.88, respectively).

**2) Loss Functions:** Regarding the choice of loss functions [see Fig. 3(d)], the MSE loss was the most frequently used, followed by L1 and L2 losses. Instead of MSE and L2, which can be oversmoothing [17], [94], some studies chose L1 loss [12], [48], [50], [73] to facilitate convergence and produce sharper images [50]. To enforce data fidelity, some studies minimized data consistency loss, i.e., the difference between the undersampled k-space data and the reconstructed k-space at the undersampled locations. Some minimized the MSE in k-space, or in one study, in the wavelet domain [40]. To enhance perceptual quality, a few studies minimized the difference in the image embeddings from a trained VGG16 network between ground-truth and reconstructed images [3]. Only two studies incorporated L2 regularization as a strategy to prevent overfitting [36], [102], and one study uses L1 regularization [25]. One study [95] minimized the negative of SSIM of the reconstructed image as SSIM was a key performance metric of CS reconstruction. Other performance metric-based loss functions included the normalized MSE (NMSE) [128], the normalized root MSE (NRMSE) [20], and the mean absolute error (MAE) [35], [39]. For probabilistic deep learning models, the loss function was based upon maximum *a posteriori* [99] or the Kullback–Leibler divergence between the latent encodings for reconstructed and ground-truth image distribution [58]. The loss functions with increased usage over time were L2, data consistency loss, and RMSE (see Table 4 in the Supplementary Material). Altogether, MSE was the most prevalent loss function, and recent deep-learning-based CS-MRI developments have explored the diversity of loss function choices.

Various studies integrated multiple loss functions to utilize the merits of them jointly [see Fig. 3(e)]. To illustrate, DAGAN [3] minimized the MSE in both image and k-space.

The VGG16-based loss function was added to improve the perceptual quality. The GAN-based adversarial loss was integrated to generate photorealistic images. Ablation experiments showed that each loss function was essential for DAGAN performance. Despite the advantages of multiple loss functions for the model training, its application did not change over time (correlation = 0.02). This may be because the training process was complicated by the need to balance the weightings of different loss components using the weighting hyperparameters.

Among the optimizers that apply the gradient of the loss function to update model parameters [see Fig. 3(c)], the most used was the Adam (65.2%), with increasing popularity over time (correlation = 0.95), followed by the stochastic gradient descent (SGD) (9.8%). In contrast, RMSProp and gradient descent with momentum were used less frequently.

**3) Input Characteristics:** To process input MR images, the predominant method operated on 2-D complex signals from the image domain [see Fig. 3(f)]. However, while raw MR signals are complex numbers, most deep learning frameworks do not support complex number calculations [102]. One solution is to only focus on the magnitude of the complex signals (14.1% of the studies). More commonly (60.9%), in the input layer of the neural network, one channel processed the real part of the MR signals, the other the imaginary part. Alternatively, the two channels can be used to process the magnitude and phase of the complex number signals [17], [48]. However, this magnitude–phase split has no benefits over the real–imaginary split [17]. Consequently, real–imaginary split dominates deep-learning-based CS-MRI model designs.

However, such a real–imaginary split may not reflect the phase information of the complex signals [102]. To tackle this issue, complex convolution [39] convolves complex numbers using separate channels for real and imaginary images (see Section II-F in the Supplementary Material), as adopted by subsequent studies [41], [74], [78], [92]. Complex convolution performance exceeded that of normal real-valued convolution [74] and networks that process magnitude images only [41]. However, calculations of complex numbers using real-valued channels

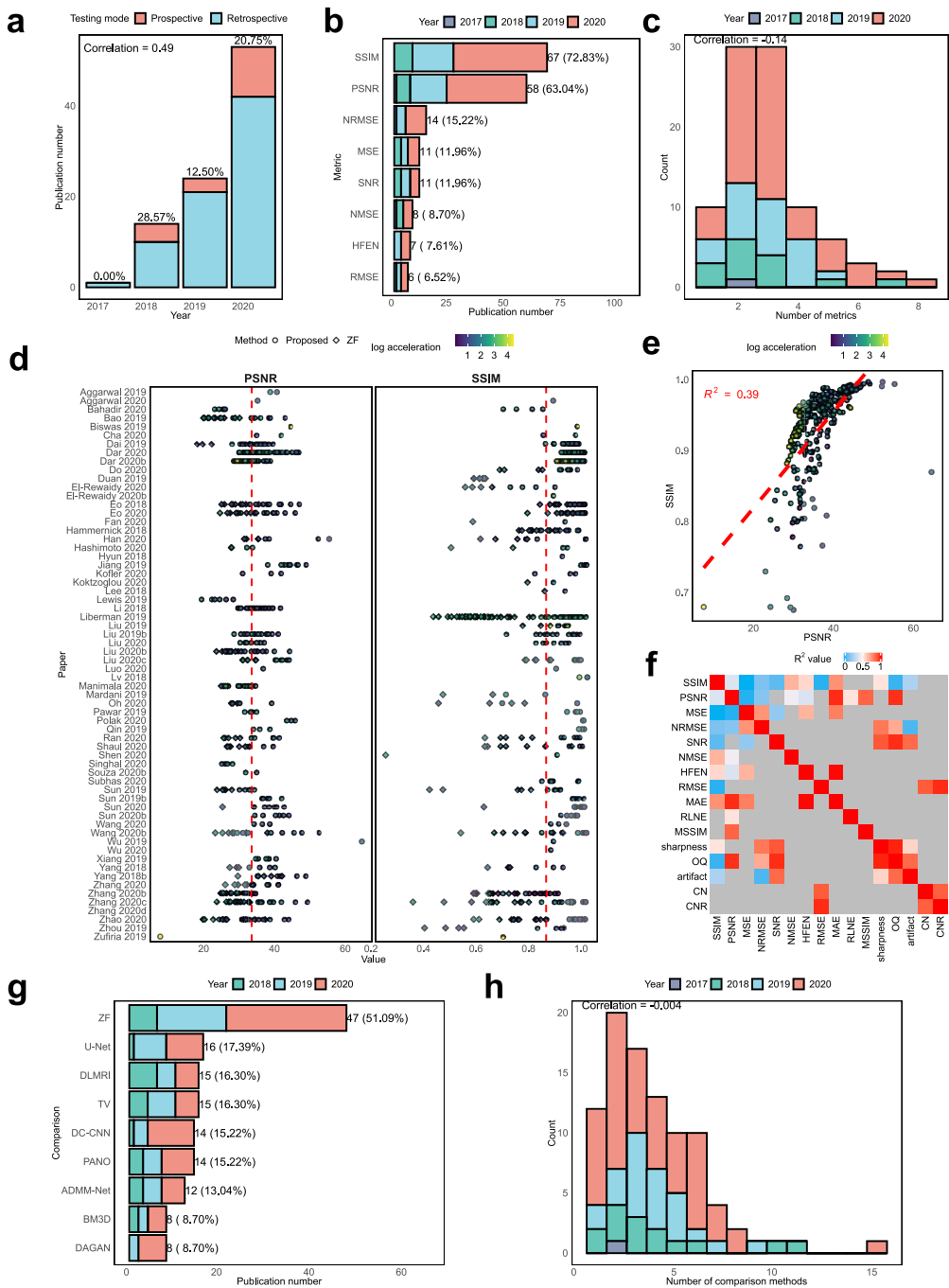


**Fig. 4.** Evaluation of the model performance. (a) Number of publications that applied prospective and retrospective undersampling over time. The proportion of models using prospective undersampling is in the text above each bar. (b) Metrics used by different studies.

**Abbreviations:** SSIM: structural similarity index; PSNR: peak signal-to-noise ratio; NRMSE: normalized root mean square error; MSE: mean square error; SNR: signal-to-noise ratio; NMSE: normalized mean square error; HFEN: high-frequency error norm; and RMSE: root mean square error. (c) Number of metrics used by different studies to evaluate model performance. The correlation of the number of metrics with time is shown in the top left corner. (d) PSNR and SSIM of the model performance across all the studies that provided performance statistics. Each dot represents the performance at a particular metric at a particular acceleration ratio using a particular method in a study. The red dashed line represents the mean of SSIM and PSNR across all studies over all acceleration ratios. (e) PSNR values of each model are plotted along the x-axis and the corresponding SSIM values along the y-axis. Each dot represents one model at a particular acceleration ratio. (f) Heatmap showing the  $R^2$  value between a pair of metrics. The gray region indicates where the  $R^2$  value is not available due to small sample sizes. Abbreviations: MAE: mean absolute error; RLNE: relative L2 norm error; MSSIM: mean structural similarity index map; OQ: overall quality; CN: contrast difference; and CNR: contrast-to-noise ratio. (g) Comparison methods used by different studies. (h) Number of comparison methods used by different studies. Abbreviations: ZF: zero filling; TV: total variation; DC-CNN: deep cascaded convolutional neural network; PANO: patch-based nonlocal operator; ADMM-Net: alternating direction method of multipliers; DLMRI: dictionary learning MRI; BM3D: block matching 3-D; and DAGAN: dealiasing generative adversarial network.

may not be applicable for other computational layers of the neural networks, e.g., batch normalization. The solution [74], [78] is radial batch normalization, that is, performing batch normalization on the magnitude image only, but the phase information is ignored. Despite attempts to circumvent complex-valued calculations, support for complex-valued operations is still an unmet need in deep learning frameworks.

*4) Other Features:* We next assessed the reproducibility of deep learning models by considering whether the dataset and source code were accessible [105]. 40.2% of the studies were “hard to reproduce,” which increased in proportion over time [correlation = 0.84; see Fig. 3(f)]. Moreover, the computation time or the parameter number did not change significantly over time ( $p = 0.38$  and  $p = 0.50$ , respectively) [see Fig. 3(g) and (h)].

Having characterized the model design traits, we used them to group the studies that we reviewed into eight clusters. The GAN-based cluster featured the GAN-based CS-MRI models [see Fig. 3(i)]. The models within the “high-acceleration” cluster displayed a high-acceleration ratio and multidimensional MR image reconstruction. The “unsupervised” cluster consisted of all unsupervised learning models. The “simple ETE” cluster consisted of ETE models that mostly do not implement data consistency layer, residual learning, GAN, or parallel imaging. The UO models were subdivided into three clusters: residual UO that implemented residual learning, PI UO that implemented parallel imaging, and non-PI UO. The “others” cluster consisted of studies with diverse traits. We have, therefore, established an unbiased classification system to characterize the architectural traits of CS-MRI models.

### C. Evaluation Metrics

We also compared how different studies evaluated the performance of their reconstruction models. CS-MRI models are tested by reconstructing undersampled images and comparing the reconstructed images with the ground truth. Undersampling can be retrospective, that is, undersampling the already acquired MR images. Prospective undersampling means collecting the undersampled k-space signals directly from the MR scanners and can better reflect performance in a real-life situation. Compared with prospective undersampling, retrospective undersampling is more financially and logically feasible [5], and is implemented in 93.5% of the studies [see Fig. 4(a)].

To compare the reconstructed images with the ground truth, most studies reported the structural similarity index measure (SSIM) and the peak signal-to-noise ratio (PSNR) [see Fig. 4(b)]. Fewer used NRMSE, MSE, and the signal-to-noise ratio (SNR). NRMSE and SSIM became more popular over time, whereas PSNR and NMSE decreased in popularity (see Table 5 in the Supplementary Material). These metrics were quantitative, i.e., a defined algorithm that computes the similarity between the reconstructed and ground-truth images. In contrast, qualitative

metrics—measures without a clearly defined mathematical expression, including the rating scores by human observers and segmentation-based scoring—are used less frequently. The most popular qualitative metrics were image sharpness (6.52%), overall quality (OQ) (4.35%), end-diastolic volume, ejection fraction, and end-systolic volume as obtained by segmentation (3.26%) and Likert scale (3.26%). Thus, quantitative metrics, such as SSIM, PSNR, and NRMSE, were the most prevalent.

Most of the studies reported at least two metrics to provide alternative performance quantifications [see Fig. 4(c)]. Across all the acceleration ratios and reported metric performance [see Fig. 4(d)], we interrogated the redundancy of metrics by using one metric to predict the performance of another via linear regression. In Fig. 4(e), the  $R^2$  value between SSIM and PSNR is low, suggesting a nonlinear relationship. For low model performance, i.e., low PSNR and SSIM values, SSIM was more sensitive to changes in model performance than PSNR. In contrast, for high-performing models, PSNR was more sensitive. The results imply that PSNR and SSIM were unlikely redundant pairs of metrics as each of them may be most sensitive to different performance levels.

Likewise, some quantitative metrics were not correlated, e.g., between SSIM, PSNR, and MSE (see Fig. 4(f), and Table 7 in the Supplementary Material), though MSE, NRMSE, and NMSE are more closely related. The most highly correlated quantitative metrics are high-frequency error norm (HFEN), MAE, PSNR, and MAE. Besides, many qualitative metrics were more linearly related, including sharpness, OQ, artifact, contrast difference (CN), and the contrast-to-noise ratio (CNR). Some quantitative and qualitative metrics also correlated, including RMSE and CNR, SNR and OQ, PSNR and OQ, and SNR and sharpness. However, this spuriously high similarity may arise because fewer studies reported qualitative than quantitative metrics. Despite the difficulty of interpreting the qualitative metrics, quantitative metrics, e.g., SSIM, PSNR, and MSE, were not linearly dependent. This cautions future research against relying upon a single metric to assess model performance.

To fully evaluate the performance of a deep learning model, 51.9% of studies compared the model performance with zero-filling, which represents the baseline reconstruction results. This involves filling the nonsampled k-space locations with zeros. Many studies also demonstrated the superiority of their models to other state-of-the-art techniques. Typical comparison techniques included U-Net, such as architectures, DC-CNN [10], ADMM-Net [64], and DAGAN [3] [see Fig. 4(g)]. Various studies also compared the performance to traditional techniques, including DLMRI [42], TV [2], PANO [139], and BM3D [140]. Increasingly popular comparison methods included DC-CNN, U-Net, and GRAPPA [141], but kt-SLR [142] was becoming less popular (see Table 6 in the Supplementary Material). Besides, 87.0% of the studies reported two or more comparison methods [see Fig. 4(h)].

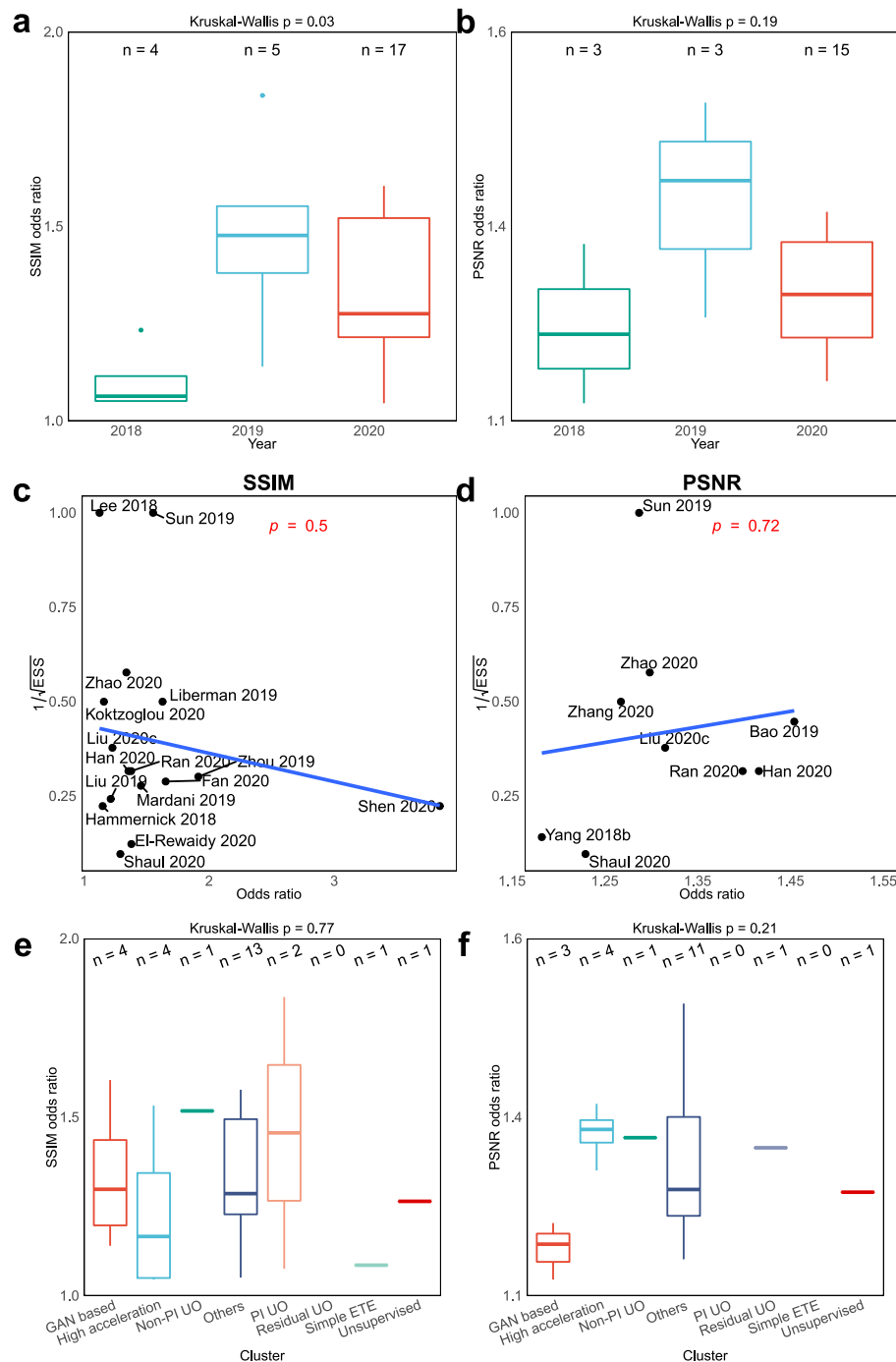


**Fig. 5. Performance improvement over the zero-filled baseline reconstruction. (a)** Odds' ratio of the SSIM improvement over time. The number of models assessed for each year group is shown above the boxes. **(b)** Odds' ratio of the PSNR improvement over time. **(c)** Deeks' test using the SSIM odds' ratio. **(d)** Deeks' test using the PSNR odds' ratio. **(e)** Odds' ratio of the SSIM improvement by clusters. **(f)** Odds' ratio of the PSNR improvement by clusters.

Therefore, many studies benchmarked their models against zero-filling, U-Net, TV, and DC-CNN.

#### D. Performance

Having assessed the model design traits and performance evaluation methods, we explored which design trait was associated with higher performance.

We quantified the performance of each model by the odds' ratio of improvement in either SSIM or PSNR over zero-filling. SSIM or PSNR odds' ratios did not change significantly over time [see Fig. 5(a) and (b)]. On the reported improvements, Deeks' test did not reveal publication bias [see Fig. 5(c) and (d)]. Across different clusters of models established earlier [see Fig. 3(i)],

the performance improvement was not significantly different [see Fig. 5(e) and (f)]. Furthermore, none of the design traits was significantly linked to performance improvement (see Table 8 in the Supplementary Material). The failure of detecting significant traits may be because performance comparison among different models was confounded by the disparity of dataset and evaluation metrics among them. Nevertheless, comparing the unadjusted  $p$ -values suggested that using the Adam optimizer may lead to higher performance, and using a U-Net, such as architecture and GAN, may lead to lower performance. A higher acceleration ratio was linked to higher SSIM improvement, probably because SSIM was the most sensitive to low-performing models [see Fig. 4(e)], and the raising acceleration ratio tended to reduce performance.

Taken together, we have pioneered the meta-analysis framework, summarized the model design traits, analyzed the developmental trend, and established a classification network for deep-learning-based CS-MRI techniques, forming a comprehensive guide for future research.

## VI. CHALLENGES

Although deep-learning-based CS-MRI techniques have advanced rapidly, they still suffer from limitations of the deep learning algorithms, most importantly, the dependence on large training data [11], [143]–[146]. Transfer learning may tackle this problem [36], [130]. With transfer learning, the models are trained on a source domain, in which training data are abundant, such as natural images. Subsequently, model parameters are fine-tuned in the target domain, in which the reconstruction is required, but the training data are scarce. Using transfer learning, models trained with 4000 natural images, perform as well as the same models trained with MR images [36]. Hence, transfer learning may address the demand for large training samples.

Another issue with deep-learning-based CS-MRI models is their generalizability to different datasets or applications. A few studies report robust performance of the models across different datasets and noise levels [21], [27], [98], [128]. However, one study shows better performance in T1 weighted images compared with FLAIR MR images [8], and another displays higher reconstruction errors in fat-containing regions [147]. Furthermore, without transfer learning, deep learning models trained on natural or T1 weighted images cannot maintain equal performance on T2 weighted images. These results indicate that the same deep-learning-based CS-MRI models may not display similar performance across different MR scanning sequences or anatomical regions. This is consistent with the instability of some deep-learning-based methods, e.g., VN, DAGAN, and DC-CNN upon small perturbations of the input image [140].

While deep learning models have a much shorter reconstruction time compared to traditional CS

techniques [3], [10], they require a long training time [143], [149]. This is exacerbated by the need for hyperparameter tuning to select the best-performing models [43], [60], [70], [150], [151], as no theories currently govern deep learning model selection [143]. Despite their superior performance over traditional CS techniques, motion artifacts may not be effectively removed by deep learning models [9], [41], [120]. Therefore, computational challenges exist toward developing a universally applicable deep-learning-based CS-MRI algorithm.

This systematic review and meta-analysis focused on how much a deep learning model improved beyond zero-filling reconstruction. However, such a comparison is challenging given that different models were tested on different datasets, metrics, and acceleration ratios. Furthermore, we did not quantitatively explore the reconstruction time to identify the most computationally efficient models because not all models were implemented on the same computing platform. We also did not analyze the overfitting properties, i.e., the discrepancy in performance between the training and testing datasets. This is because most studies reported performance on testing but not training datasets. Hence, to facilitate the future systematic review, we encourage future studies to test their model performance on commonly used datasets (human connectome projects, fastMRI, and IXI in Table 3) and metrics (PSNR and SSIM) and report performance on both training and testing datasets.

## VII. CONCLUSION AND OUTLOOK

With the rapid rise of deep learning in computer vision, the past four years have witnessed substantial changes in the landscape of deep-learning-based CS-MRI techniques. To summarize these developments, we have conducted a systematic review and meta-analysis. We have introduced a comprehensive analysis framework based on the CLAIM criteria, summarized the typical deep neural network architectures in CS-MRI, compared their performance, and evaluated their strengths and limitations. Earlier deep-learning-based CS-MRI techniques have highlighted the developments of neural network architectures, including the data consistency layer, VN, GAN, residual learning, cross-domain networks, and so on. More recently, the redundancy of MR images is explored, either across different contrasts, higher imaging dimensions, or parallel imaging channels. However, with the increasing diversity of deep-learning-based CS-MRI techniques, finding an appropriate and fair comparison benchmark is challenging. Nonetheless, we believe that the excitement of this field lies not only in improving beyond benchmark works but also in creating new benchmarks for unexplored applications of CS-MRI. With this goal, efforts, and drives among the deep learning community, milestones are set for faster and more accurate reconstruction performance. These developments may inspire other MRI applications,

such as MRI fingerprinting [152], [153], by synthesizing a quantitative map of tissue properties from MR signal evolution over the signal acquisition trajectory. Therefore, we can envisage that the development of deep-learning-based fast CS-MRI will usher in a new era of digital

healthcare and personalized medicine, which will be equipped with high throughput and low-cost imaging, and more reliable quantitative imaging biomarker extraction and analysis. ■

## REFERENCES

- [1] K. G. Hollingsworth, "Reducing acquisition time in clinical MRI by data undersampling and compressed sensing reconstruction," *Phys. Med. Biol.*, vol. 60, no. 21, pp. R297–R322, Oct. 2015, doi: [10.1088/0031-9115/60/21/R297](https://doi.org/10.1088/0031-9115/60/21/R297).
- [2] M. Lustig, D. Donoho, and J. M. Pauly, "Sparse MRI: The application of compressed sensing for rapid MR imaging," *Magn. Reson. Med.*, vol. 58, no. 6, pp. 1182–1195, Dec. 2007, doi: [10.1002/mrm.21391](https://doi.org/10.1002/mrm.21391).
- [3] G. Yang et al., "DAGAN: Deep de-aliasing generative adversarial networks for fast compressed sensing MRI reconstruction," *IEEE Trans. Med. Imag.*, vol. 37, no. 6, pp. 1310–1321, Jun. 2017, doi: [10.1109/TMI.2017.2785879](https://doi.org/10.1109/TMI.2017.2785879).
- [4] P. Suetens, *Fundamentals of Medical Imaging*, 2nd ed. New York, NY, USA: Cambridge Univ. Press, 2009.
- [5] O. N. Jaspan, R. Fleysher, and M. L. Lipton, "Compressed sensing MRI: A review of the clinical literature," *Brit. J. Radiol.*, vol. 88, no. 1056, Dec. 2015, Art. no. 20150487, doi: [10.1259/bjr.20150487](https://doi.org/10.1259/bjr.20150487).
- [6] M. J. Fair, P. D. Gatehouse, E. V. R. DiBella, and D. N. Firmin, "A review of 3D first-pass, whole-heart, myocardial perfusion cardiovascular magnetic resonance," *J. Cardiovascular Magn. Reson.*, vol. 17, p. 68, Aug. 2015, doi: [10.1186/s12968-015-0162-9](https://doi.org/10.1186/s12968-015-0162-9).
- [7] S. Vishnukumar and M. Wilscy, "Single image super-resolution based on compressive sensing and improved TV minimization sparse recovery," *Opt. Commun.*, vol. 404, pp. 80–93, Dec. 2017, doi: [10.1016/j.optcom.2017.05.074](https://doi.org/10.1016/j.optcom.2017.05.074).
- [8] T. Eo, Y. Jun, T. Kim, J. Jang, H.-J. Lee, and D. Hwang, "KIKI-Net: Cross-domain convolutional neural networks for reconstructing undersampled magnetic resonance images," *Magn. Reson. Med.*, vol. 80, no. 5, pp. 2188–2201, Nov. 2018, doi: [10.1002/mrm.27201](https://doi.org/10.1002/mrm.27201).
- [9] C. Qin, J. Schlemper, J. Caballero, A. N. Price, J. V. Hajnal, and D. Rueckert, "Convolutional recurrent neural networks for dynamic MR image reconstruction," *IEEE Trans. Med. Imag.*, vol. 38, no. 1, pp. 280–290, Jan. 2019, doi: [10.1109/TMI.2018.2863670](https://doi.org/10.1109/TMI.2018.2863670).
- [10] J. Schlemper, J. Caballero, J. V. Hajnal, A. N. Price, and D. Rueckert, "A deep cascade of convolutional neural networks for dynamic MR image reconstruction," *IEEE Trans. Med. Imag.*, vol. 37, no. 2, pp. 491–503, Feb. 2018, doi: [10.1109/TMI.2017.2760978](https://doi.org/10.1109/TMI.2017.2760978).
- [11] K.-H. Yu, A. L. Beam, and I. S. Kohane, "Artificial intelligence in healthcare," *Nature Biomed. Eng.*, vol. 2, no. 10, pp. 719–731, Oct. 2018, doi: [10.1038/s41551-018-0305-z](https://doi.org/10.1038/s41551-018-0305-z).
- [12] G. Liberman and B. A. Poser, "Minimal linear networks for magnetic resonance image reconstruction," *Sci. Rep.*, vol. 9, no. 1, p. 19527, Dec. 2019, doi: [10.1038/s41598-019-55763-x](https://doi.org/10.1038/s41598-019-55763-x).
- [13] D. Liang, J. Cheng, Z. Ke, and L. Ying, "Deep MRI reconstruction: Unrolled optimization algorithms meet neural networks," 2019, *arXiv:1907.11711*.
- [14] D. Liang, J. Cheng, Z. Ke, and L. Ying, "Deep magnetic resonance image reconstruction: Inverse problems meet neural networks," *IEEE Signal Process. Mag.*, vol. 37, no. 1, pp. 141–151, Jan. 2020, doi: [10.1109/MSP.2019.2950557](https://doi.org/10.1109/MSP.2019.2950557).
- [15] H.-M. Zhang and B. Dong, "A review on deep learning in medical image reconstruction," *J. Oper. Res. Soc. China*, vol. 8, no. 2, pp. 311–340, Jun. 2020, doi: [10.1007/s40305-019-00287-4](https://doi.org/10.1007/s40305-019-00287-4).
- [16] O. Ronneberger, P. Fischer, and T. Brox, "U-Net: Convolutional networks for biomedical image segmentation," May 2015, *arXiv:1505.04597*. Accessed: Dec. 16, 2020.
- [17] D. Lee, J. Yoo, S. Tak, and J. Ye, "Deep residual learning for accelerated MRI using magnitude and phase networks," *IEEE Trans. Biomed. Eng.*, vol. 65, no. 9, pp. 1985–1995, Sep. 2018, doi: [10.1109/TBME.2018.2821699](https://doi.org/10.1109/TBME.2018.2821699).
- [18] Y. Wu, Y. Ma, J. Du, and L. Xing, "Accelerating quantitative MR imaging with the incorporation of B1 compensation using deep learning," *Magn. Reson. Imag.*, vol. 72, pp. 78–86, Oct. 2020, doi: [10.1016/j.mri.2020.06.011](https://doi.org/10.1016/j.mri.2020.06.011).
- [19] S. Diamond, V. Sitzmann, F. Heide, and G. Wetzstein, "Unrolled optimization with deep priors," 2017, *arXiv:1705.08041*.
- [20] Y. Liu, Q. Liu, M. Zhang, Q. Yang, S. Wang, and D. Liang, "IFR-Net: Iterative feature refinement network for compressed sensing MRI," *IEEE Trans. Comput. Imag.*, vol. 6, pp. 434–446, 2020, doi: [10.1109/TCI.2019.2956877](https://doi.org/10.1109/TCI.2019.2956877).
- [21] Y. Yang, J. Sun, H. Li, and Z. Xu, "ADMM-CSNet: A deep learning approach for image compressive sensing," *IEEE Trans. Pattern Anal. Mach. Intell.*, vol. 42, no. 3, pp. 521–538, Mar. 2020, doi: [10.1109/TPAMI.2018.2883941](https://doi.org/10.1109/TPAMI.2018.2883941).
- [22] H. K. Aggarwal, M. P. Mani, and M. Jacob, "MoDL: Model-based deep learning architecture for inverse problems," *IEEE Trans. Med. Imag.*, vol. 38, no. 2, pp. 394–405, Feb. 2019, doi: [10.1109/TMI.2018.2865356](https://doi.org/10.1109/TMI.2018.2865356).
- [23] W. Zeng, J. Peng, S. Wang, and Q. Liu, "A comparative study of CNN-based super-resolution methods in MRI reconstruction and its beyond," *Signal Process., Image Commun.*, vol. 81, Feb. 2020, Art. no. 115701, doi: [10.1016/j.image.2019.115701](https://doi.org/10.1016/j.image.2019.115701).
- [24] J. Lewis D., V. Singh, and A. Majumdar, "Solving inverse problems in imaging via deep dictionary learning," *IEEE Access*, vol. 7, pp. 37039–37049, 2019, doi: [10.1109/ACCESS.2018.2881492](https://doi.org/10.1109/ACCESS.2018.2881492).
- [25] V. Singh and A. Majumdar, "Reconstructing multi-echo magnetic resonance images via structured deep dictionary learning," *Neurocomputing*, vol. 408, pp. 135–143, Sep. 2020, doi: [10.1016/j.neucom.2019.11.107](https://doi.org/10.1016/j.neucom.2019.11.107).
- [26] T. Lu et al., "pFISTA-SENSE-ResNet for parallel MRI reconstruction," *J. Magn. Reson.*, vol. 318, Sep. 2020, Art. no. 106790, doi: [10.1016/j.jmr.2020.106790](https://doi.org/10.1016/j.jmr.2020.106790).
- [27] X. Zhang, Q. Lian, Y. Yang, and Y. Su, "A deep unrolling network inspired by total variation for compressed sensing MRI," *Digit. Signal Process.*, vol. 107, Dec. 2020, Art. no. 102856, doi: [10.1016/j.dsp.2020.102856](https://doi.org/10.1016/j.dsp.2020.102856).
- [28] A. Pramanik, H. K. Aggarwal, and M. Jacob, "Deep generalization of structured low-rank algorithms (deep-SLR)," *IEEE Trans. Med. Imag.*, vol. 39, no. 12, pp. 4186–4197, Dec. 2020, doi: [10.1109/tmi.2020.3014581](https://doi.org/10.1109/tmi.2020.3014581).
- [29] S. Biswas, H. K. Aggarwal, and M. Jacob, "Dynamic MRI using model-based deep learning and SToRM priors: MoDL-SToRM," *Magn. Reson. Med.*, vol. 82, no. 1, pp. 485–494, 2019, doi: [10.1002/mrm.27706](https://doi.org/10.1002/mrm.27706).
- [30] K. Hamernik et al., "Learning a variational network for reconstruction of accelerated MRI data," *Magn. Reson. Med.*, vol. 79, no. 6, pp. 3055–3071, Jun. 2018, doi: [10.1002/mrm.26977](https://doi.org/10.1002/mrm.26977).
- [31] Q. Liu, Q. Yang, H. Cheng, S. Wang, M. Zhang, and D. Liang, "Highly undersampled magnetic resonance imaging reconstruction using autoencoding priors," *Magn. Reson. Med.*, vol. 83, no. 1, pp. 322–336, Jan. 2020, doi: [10.1002/mrm.27921](https://doi.org/10.1002/mrm.27921).
- [32] S. A. H. Hosseini et al., "Accelerated coronary MRI with sRAKI: A database-free self-consistent neural network k-space reconstruction for arbitrary undersampling," *PLoS ONE*, vol. 15, no. 2, Feb. 2020, Art. no. e0229418, doi: [10.1371/journal.pone.0229418](https://doi.org/10.1371/journal.pone.0229418).
- [33] L. Sun, Y. Wu, Z. Fan, X. Ding, Y. Huang, and J. Paisley, "A deep error correction network for compressed sensing MRI," *BMC Biomed. Eng.*, vol. 2, no. 1, pp. 1–12, Dec. 2020, doi: [10.1186/s42490-020-0037-5](https://doi.org/10.1186/s42490-020-0037-5).
- [34] M. Zhang et al., "High-dimensional embedding network derived prior for compressive sensing MRI reconstruction," *Med. Image Anal.*, vol. 64, Aug. 2020, Art. no. 101717, doi: [10.1016/j.media.2020.101717](https://doi.org/10.1016/j.media.2020.101717).
- [35] K. Zeng, Y. Yang, G. Xiao, and Z. Chen, "A very deep densely connected network for compressed sensing MRI," *IEEE Access*, vol. 7, pp. 85430–85439, 2019, doi: [10.1109/ACCESS.2019.2924604](https://doi.org/10.1109/ACCESS.2019.2924604).
- [36] S. U. H. Dar, M. Özbeý, A. B. Çatlı, and T. Çukur, "A transfer-learning approach for accelerated MRI using deep neural networks," *Magn. Reson. Med.*, vol. 84, no. 2, pp. 663–685, Aug. 2020, doi: [10.1002/mrm.28148](https://doi.org/10.1002/mrm.28148).
- [37] M. O. Malavé et al., "Reconstruction of undersampled 3D non-Cartesian image-based navigators for coronary MRA using an unrolled deep learning model," *Magn. Reson. Med.*, vol. 84, no. 2, pp. 800–812, Aug. 2020, doi: [10.1002/mrm.28177](https://doi.org/10.1002/mrm.28177).
- [38] M. Ran et al., "MD-Recon-Net: A parallel dual-domain convolutional neural network for compressed sensing MRI," *IEEE Trans. Radiat. Plasma Med. Sci.*, vol. 5, no. 1, pp. 120–135, Jan. 2021, doi: [10.1109/trpms.2020.2991877](https://doi.org/10.1109/trpms.2020.2991877).
- [39] S. Wang et al., "DeepcomplexMRI: Exploiting deep residual network for fast parallel MRI imaging with complex convolution," *Magn. Reson. Imag.*, vol. 68, pp. 136–147, May 2020, doi: [10.1016/j.mri.2020.02.002](https://doi.org/10.1016/j.mri.2020.02.002).
- [40] Z. Wang, H. Jiang, H. Du, J. Xu, and B. Qiu, "IKWI-Net: A cross-domain convolutional neural network for undersampled magnetic resonance image reconstruction," *Magn. Reson. Imag.*, vol. 73, pp. 1–10, Nov. 2020, doi: [10.1016/j.mri.2020.06.015](https://doi.org/10.1016/j.mri.2020.06.015).
- [41] D. Shen et al., "Rapid reconstruction of highly undersampled, non-Cartesian real-time cine k-space data using a perceptual complex neural network (PCNN)," *NMR Biomed.*, vol. 34, no. 1, Jan. 2021, Art. no. e4405, doi: [10.1002/nbm.4405](https://doi.org/10.1002/nbm.4405).
- [42] S. Ravishankar and Y. Bresler, "MR image reconstruction from highly undersampled k-space data by dictionary learning," *IEEE Trans. Med. Imag.*, vol. 30, no. 5, pp. 1028–1041, May 2011, doi: [10.1109/TMI.2010.2090538](https://doi.org/10.1109/TMI.2010.2090538).
- [43] F. Chen et al., "Variable-density single-shot fast spin-echo MRI with deep learning reconstruction by using variational networks," *Radiology*, vol. 289, no. 2, pp. 366–373, Nov. 2018, doi: [10.1148/radiol.2018180445](https://doi.org/10.1148/radiol.2018180445).
- [44] D. Polak et al., "Joint multi-contrast variational network reconstruction (JVN) with application to rapid 2D and 3D imaging," *Magn. Reson. Med.*, vol. 84, no. 3, pp. 1456–1469, Sep. 2020, doi: [10.1002/mrm.28219](https://doi.org/10.1002/mrm.28219).
- [45] V. Vishnevskiy, J. Walheim, and S. Kozerke, "Deep variational network for rapid 4D flow MRI reconstruction," *Nature Mach. Intell.*, vol. 2, no. 4, pp. 228–235, Apr. 2020, doi: [10.1038/s42256-020-0165-6](https://doi.org/10.1038/s42256-020-0165-6).
- [46] H. K. Aggarwal and M. Jacob, "J-MoDL: Joint model-based deep learning for optimized sampling and reconstruction," *IEEE J. Sel. Topics Signal Process.*, vol. 14, no. 6, pp. 1151–1162, Oct. 2020, doi: [10.1109/jstsp.2020.3004094](https://doi.org/10.1109/jstsp.2020.3004094).

- [47] L. Bao *et al.*, “Undersampled MR image reconstruction using an enhanced recursive residual network,” *J. Magn. Reson.*, vol. 305, pp. 232–246, Aug. 2019, doi: [10.1016/j.jmr.2019.07.020](https://doi.org/10.1016/j.jmr.2019.07.020).
- [48] S. U. H. Dar, M. Yurt, M. Shahdloo, M. E. Ildiz, B. Tinaz, and T. Cukur, “Prior-guided image reconstruction for accelerated multi-contrast MRI via generative adversarial networks,” *IEEE J. Sel. Topics Signal Process.*, vol. 14, no. 6, pp. 1072–1087, Oct. 2020, doi: [10.1109/jstsp.2020.3001737](https://doi.org/10.1109/jstsp.2020.3001737).
- [49] C. M. Hyun, H. P Kim, S. M. Lee, S. Lee, and J. K. Seo, “Deep learning for undersampled MRI reconstruction,” *Phys. Med. Biol.*, vol. 63, no. 13, 2018, Art. no. 135007, doi: [10.1088/1361-6560/aac71a](https://doi.org/10.1088/1361-6560/aac71a).
- [50] M. Mardani *et al.*, “Deep generative adversarial neural networks for compressive sensing MRI,” *IEEE Trans. Med. Imag.*, vol. 38, no. 1, pp. 167–179, Jan. 2019, doi: [10.1109/TMI.2018.2858752](https://doi.org/10.1109/TMI.2018.2858752).
- [51] Y. Wu, Y. Ma, J. Liu, J. Du, and L. Xing, “Self-attention convolutional neural network for improved MR image reconstruction,” *Inf. Sci.*, vol. 490, pp. 317–328, Jul. 2019, doi: [10.1016/j.ins.2019.03.080](https://doi.org/10.1016/j.ins.2019.03.080).
- [52] D. Zhao, F. Zhao, and Y. Gan, “Reference-driven compressed sensing MR image reconstruction using deep convolutional neural networks without pre-training,” *Sensors*, vol. 20, no. 1, Jan. 2020, Art. no. 1, doi: [10.3390/s20010308](https://doi.org/10.3390/s20010308).
- [53] D. Ulyanov, A. Vedaldi, and V. Lempitsky, “Deep image prior,” *Int. J. Comput. Vis.*, vol. 128, no. 7, pp. 1867–1888, Jul. 2020, doi: [10.1007/s11263-020-01303-4](https://doi.org/10.1007/s11263-020-01303-4).
- [54] K. Gong, P. Han, G. E. Fakhr, C. Ma, and Q. Li, “Arterial spin labeling MR image denoising and reconstruction using unsupervised deep learning,” *NMR Biomed.*, Dec. 2019, Art. no. e4224, doi: [10.1002/nbm.4224](https://doi.org/10.1002/nbm.4224).
- [55] A. Majumdar, “An autoencoder based formulation for compressed sensing reconstruction,” *Magn. Reson. Imag.*, vol. 52, pp. 62–68, Oct. 2018, doi: [10.1016/j.mri.2018.06.003](https://doi.org/10.1016/j.mri.2018.06.003).
- [56] I. J. Goodfellow *et al.*, “Generative adversarial networks,” Jun. 2014, *arXiv:1406.2661*. Accessed: Dec. 17, 2020.
- [57] E. Cha, H. Chung, E. Y. Kim, and J. C. Ye, “Unpaired training of deep learning tMRI for flexible spatio-temporal resolution,” *IEEE Trans. Med. Imag.*, vol. 40, no. 1, pp. 166–179, Jan. 2021, doi: [10.1109/TMI.2020.3023620](https://doi.org/10.1109/TMI.2020.3023620).
- [58] V. Edupuganti, M. Mardani, S. Vasanawala, and J. Pauly, “Uncertainty quantification in deep MRI reconstruction,” *IEEE Trans. Med. Imag.*, vol. 40, no. 1, pp. 239–250, Jan. 2021, doi: [10.1109/tmi.2020.3025065](https://doi.org/10.1109/tmi.2020.3025065).
- [59] M. Jiang *et al.*, “Accelerating CS-MRI reconstruction with fine-tuning Wasserstein generative adversarial network,” *IEEE Access*, vol. 7, pp. 152347–152357, 2019, doi: [10.1109/ACCESS.2019.2948220](https://doi.org/10.1109/ACCESS.2019.2948220).
- [60] F. Liu, A. Samsonov, L. Chen, R. Kijowski, and L. Feng, “SANTIS: Sampling-augmented neural network with incoherent structure for MR image reconstruction,” *Magn. Reson. Med.*, vol. 82, no. 5, pp. 1890–1904, Nov. 2019, doi: [10.1002/mrm.27827](https://doi.org/10.1002/mrm.27827).
- [61] G. Oh, B. Sim, H. Chung, L. Sunwoo, and J. C. Ye, “Unpaired deep learning for accelerated MRI using optimal transport driven CycleGAN,” *IEEE Trans. Comput. Imag.*, vol. 6, pp. 1285–1296, 2020, doi: [10.1109/TCI.2020.3018562](https://doi.org/10.1109/TCI.2020.3018562).
- [62] T. M. Quan, T. Nguyen-Duc, and W.-K. Jeong, “Compressed sensing MRI reconstruction using a generative adversarial network with a cyclic loss,” *IEEE Trans. Med. Imag.*, vol. 37, no. 6, pp. 1488–1497, Jun. 2018, doi: [10.1109/TMI.2018.2820120](https://doi.org/10.1109/TMI.2018.2820120).
- [63] R. Shaul, I. David, O. Shirrit, and T. R. Raviv, “Subsampled brain MRI reconstruction by generative adversarial neural networks,” *Med. Image Anal.*, vol. 65, Oct. 2020, Art. no. 101747, doi: [10.1016/j.media.2020.101747](https://doi.org/10.1016/j.media.2020.101747).
- [64] Y. Yang, J. Sun, H. Li, and Z. Xu, “ADMM-Net: A deep learning approach for compressive sensing MRI,” 2017, *arXiv:1705.06869*.
- [65] Z. Chen and Y. Tong, “Face super-resolution through Wasserstein GANs,” May 2017, *arXiv:1705.02438*. Accessed: Dec. 16, 2020.
- [66] L. Metz, B. Poole, D. Pfau, and J. Sohl-Dickstein, “Unrolled generative adversarial networks,” May 2017, *arXiv:1611.02163*. Accessed: Dec. 16, 2020.
- [67] M. Wiatrak, S. V. Albrecht, and A. Nyström, “Stabilizing generative adversarial networks: A survey,” Mar. 2020, *arXiv:1910.00927*. Accessed: Dec. 16, 2020.
- [68] M. Arjovsky, S. Chintala, and L. Bottou, “Wasserstein GAN,” Dec. 2017, *arXiv:1701.07875*. Accessed: Dec. 17, 2020.
- [69] H. Zhao, O. Gallo, I. Frosio, and J. Kautz, “Loss functions for image restoration with neural networks,” *IEEE Trans. Comput. Imag.*, vol. 3, no. 1, pp. 47–57, Mar. 2017, doi: [10.1109/TCI.2016.2644865](https://doi.org/10.1109/TCI.2016.2644865).
- [70] M. Akçakaya, S. Moeller, S. Weingärtner, and K. Ügürbil, “Scan-specific robust artificial-neural-networks for *k*-space interpolation (RAKI) reconstruction: Database-free deep learning for fast imaging,” *Magn. Reson. Med.*, vol. 81, no. 1, pp. 439–453, Jan. 2019, doi: [10.1002/mrm.27420](https://doi.org/10.1002/mrm.27420).
- [71] Y. Han, L. Sunwoo, and J. C. Ye, “*k*-Space deep learning for accelerated MRI,” *IEEE Trans. Med. Imag.*, vol. 39, no. 2, pp. 377–386, Feb. 2020, doi: [10.1109/TMI.2019.2927101](https://doi.org/10.1109/TMI.2019.2927101).
- [72] B. Zhu, J. Z. Liu, S. F. Cauley, B. R. Rosen, and M. S. Rosen, “Image reconstruction by domain-transform manifold learning,” *Nature*, vol. 555, no. 7697, pp. 487–492, Mar. 2018, doi: [10.1038/nature25988](https://doi.org/10.1038/nature25988).
- [73] T. Eo, H. Shin, Y. Jun, T. Kim, and D. Hwang, “Accelerating Cartesian MRI by domain-transform manifold learning in phase-encoding direction,” *Med. Image Anal.*, vol. 63, Jul. 2020, Art. no. 101689, doi: [10.1016/j.media.2020.101689](https://doi.org/10.1016/j.media.2020.101689).
- [74] H. El-Rewaidy *et al.*, “Deep complex convolutional network for fast reconstruction of 3D late gadolinium enhancement cardiac MRI,” *NMR Biomed.*, vol. 33, no. 7, Jul. 2020, Art. no. e4312, doi: [10.1002/nbm.4312](https://doi.org/10.1002/nbm.4312).
- [75] R. Souza *et al.*, “Dual-domain cascade of U-Nets for multi-channel magnetic resonance image reconstruction,” *Magn. Reson. Imag.*, vol. 71, pp. 140–153, Sep. 2020, doi: [10.1016/j.mri.2020.06.002](https://doi.org/10.1016/j.mri.2020.06.002).
- [76] S. Fujieda, K. Takayama, and T. Hachisuka, “Wavelet convolutional neural networks,” May 2018, *arXiv:1805.08620*. Accessed: Dec. 17, 2020.
- [77] H. El-Rewaidy *et al.*, “Multi-domain convolutional neural network (MD-CNN) for radial reconstruction of dynamic cardiac MRI,” *Magn. Reson. Med.*, vol. 85, no. 3, pp. 1195–1208, Mar. 2021, doi: [10.1002/mrm.28485](https://doi.org/10.1002/mrm.28485).
- [78] L. Sun *et al.*, “A dual-domain deep lattice network for rapid MRI reconstruction,” *Neurocomputing*, vol. 397, pp. 94–107, Jul. 2020, doi: [10.1016/j.neucom.2020.01.063](https://doi.org/10.1016/j.neucom.2020.01.063).
- [79] E. Cha, G. Oh, and J. C. Ye, “Geometric approaches to increase the expressivity of deep neural networks for MR reconstruction,” *IEEE J. Sel. Topics Signal Process.*, vol. 14, no. 6, pp. 1292–1305, Oct. 2020, doi: [10.1109/jstsp.2020.2982777](https://doi.org/10.1109/jstsp.2020.2982777).
- [80] Z. Yuan *et al.*, “SARA-GAN: Self-attention and relative average discriminator based generative adversarial networks for fast compressed sensing MRI reconstruction,” *Frontiers Neuroinform.*, vol. 14, p. 58, Nov. 2020, doi: [10.3389/fninf.2020.611666](https://doi.org/10.3389/fninf.2020.611666).
- [81] W. Zhou, H. Du, W. Mei, and L. Fang, “Spatial orthogonal attention generative adversarial network for MRI reconstruction,” *Med. Phys.*, vol. 48, no. 2, pp. 627–639, Feb. 2021, doi: [10.1002/mp.14509](https://doi.org/10.1002/mp.14509).
- [82] J. Huang, C. Chen, and L. Axel, “Fast multi-contrast MRI reconstruction,” *Magn. Reson. Imag.*, vol. 32, no. 10, pp. 1344–1352, Dec. 2014, doi: [10.1016/j.mri.2014.08.025](https://doi.org/10.1016/j.mri.2014.08.025).
- [83] L. Xiang *et al.*, “Deep-learning-based multi-modal fusion for fast MR reconstruction,” *IEEE Trans. Biomed. Eng.*, vol. 66, no. 7, pp. 2105–2114, Jul. 2019, doi: [10.1109/TBME.2018.2883958](https://doi.org/10.1109/TBME.2018.2883958).
- [84] L. Sun, Z. Fan, X. Fu, Y. Huang, X. Ding, and J. Paisley, “A deep information sharing network for multi-contrast compressed sensing MRI reconstruction,” *IEEE Trans. Image Process.*, vol. 28, no. 12, pp. 6141–6153, Dec. 2019, doi: [10.1109/TIP.2019.2925288](https://doi.org/10.1109/TIP.2019.2925288).
- [85] W. Do, S. Seo, Y. Han, J. C. Ye, S. H. Choi, and S. Park, “Reconstruction of multicontrast MR images through deep learning,” *Med. Phys.*, vol. 47, no. 3, pp. 983–997, Mar. 2020, doi: [10.1002/mp.14006](https://doi.org/10.1002/mp.14006).
- [86] A. Kofler, M. Dewey, T. Schaeffter, C. Wald, and C. Kolbitsch, “Spatio-temporal deep learning-based undersampling artefact reduction for 2D radial cine MRI with limited training data,” *IEEE Trans. Med. Imag.*, vol. 39, no. 3, pp. 703–717, Mar. 2020, doi: [10.1109/TMI.2019.2930318](https://doi.org/10.1109/TMI.2019.2930318).
- [87] L. Fan *et al.*, “Rapid dealiasing of undersampled, non-Cartesian cardiac perfusion images using U-Net,” *NMR Biomed.*, vol. 33, no. 5, May 2020, Art. no. e4239, doi: [10.1002/nbm.4239](https://doi.org/10.1002/nbm.4239).
- [88] J. Liu, Y. Sun, C. Eldeniz, W. Gan, H. An, and U. S. Kamilov, “RARE: Image reconstruction using deep priors learned without groundtruth,” *IEEE J. Sel. Topics Signal Process.*, vol. 14, no. 6, pp. 1088–1099, Oct. 2020, doi: [10.1109/JSTSP2020.2998402](https://doi.org/10.1109/JSTSP2020.2998402).
- [89] C. M. Sandino, P. Lai, S. S. Vasanawala, and J. Y. Cheng, “Accelerating cardiac cine MRI using a deep learning-based ESPiRiT reconstruction,” *Magn. Reson. Med.*, vol. 85, no. 1, pp. 152–167, Jan. 2021, doi: [10.1002/mrm.28420](https://doi.org/10.1002/mrm.28420).
- [90] D. Tran, H. Wang, L. Torresani, J. Ray, Y. LeCun, and M. Paluri, “A closer look at spatiotemporal convolutions for action recognition,” in *Proc. IEEE/CVF Conf. Comput. Vis. Pattern Recognit.*, Jun. 2018, pp. 6450–6459, doi: [10.1109/CVPR.2018.00675](https://doi.org/10.1109/CVPR.2018.00675).
- [91] T. Küstner *et al.*, “CINENet: Deep learning-based 3D cardiac CINE MRI reconstruction with multi-coil complex-valued 4D spatio-temporal convolutions,” *Sci. Rep.*, vol. 10, no. 1, p. 13710, Dec. 2020, doi: [10.1038/s41598-020-70551-8](https://doi.org/10.1038/s41598-020-70551-8).
- [92] S. A. H. Hosseini, B. Yaman, S. Moeller, M. Hong, and M. Akçakaya, “Dense recurrent neural networks for accelerated MRI: History-cognizant unrolling of optimization algorithms,” *IEEE J. Sel. Topics Signal Process.*, vol. 14, no. 6, pp. 1280–1291, Oct. 2020, doi: [10.1109/JSTSP.2020.3003170](https://doi.org/10.1109/JSTSP.2020.3003170).
- [93] Z. Ke, J. Cheng, L. Ying, H. Zheng, Y. Zhu, and D. Liang, “An unsupervised deep learning method for multi-coil cine MRI,” *Phys. Med. Biol.*, vol. 65, no. 23, Dec. 2020, Art. no. 235041, doi: [10.1088/1361-6560/abaffa](https://doi.org/10.1088/1361-6560/abaffa).
- [94] M. P. Recht *et al.*, “Using deep learning to accelerate knee MRI at 3 T: Results of an interchangeability study,” *Amer. J. Roentgenol.*, vol. 215, no. 6, pp. 1421–1429, Dec. 2020, doi: [10.2214/AJR.20.23313](https://doi.org/10.2214/AJR.20.23313).
- [95] F. Chen *et al.*, “Data-driven self-calibration and reconstruction for non-Cartesian wave-encoded single-shot fast spin echo using deep learning,” *J. Magn. Reson. Imag.*, vol. 51, no. 3, pp. 841–853, Mar. 2020, doi: [10.1002/jmri.26871](https://doi.org/10.1002/jmri.26871).
- [96] R. Liu, Y. Zhang, S. Cheng, Z. Luo, and X. Fan, “A deep framework assembling principled modules for CS-MRI: Unrolling perspective, convergence behaviors, and practical modeling,” *IEEE Trans. Med. Imag.*, vol. 39, no. 12, pp. 4150–4163, Dec. 2020, doi: [10.1109/TMI.2020.3014193](https://doi.org/10.1109/TMI.2020.3014193).
- [97] K. Lønning, P. Putzky, J.-J. Sonke, L. Reneman,

- M. W. A. Caan, and M. Welling, "Recurrent inference machines for reconstructing heterogeneous MRI data," *Med. Image Anal.*, vol. 53, pp. 64–78, Apr. 2019, doi: [10.1016/j.media.2019.01.005](https://doi.org/10.1016/j.media.2019.01.005).
- [99] G. Luo, N. Zhao, W. Jiang, E. S. Hui, and P. Cao, "MRI reconstruction using deep Bayesian estimation," *Magn. Reson. Med.*, vol. 84, no. 4, pp. 2246–2261, Oct. 2020, doi: [10.1002/mrm.28274](https://doi.org/10.1002/mrm.28274).
- [100] J. Zhang et al., "Fidelity imposed network edit (FINE) for solving ill-posed image reconstruction," *NeuroImage*, vol. 211, May 2020, Art. no. 116579, doi: [10.1016/j.neuroimage.2020.116579](https://doi.org/10.1016/j.neuroimage.2020.116579).
- [101] Z. Zhou et al., "Parallel imaging and convolutional neural network combined fast MR image reconstruction: Applications in low-latency accelerated real-time imaging," *Med. Phys.*, vol. 46, no. 8, pp. 3399–3413, Aug. 2019, doi: [10.1002/mp.13628](https://doi.org/10.1002/mp.13628).
- [102] J. Montalt-Tordera, V. Muthurangun, A. Hauptmann, and J. A. Steeden, "Machine learning in magnetic resonance imaging: Image reconstruction," Dec. 2020, *arXiv:2012.05303*. Accessed: Dec. 16, 2020.
- [103] J. Mongan, L. Moy, and C. E. Kahn, "Checklist for artificial intelligence in medical imaging (CLAIM): A guide for authors and reviewers," *Radiol. Artif. Intell.*, vol. 2, no. 2, Mar. 2020, Art. no. e200029, doi: [10.1148/ryai.2020200029](https://doi.org/10.1148/ryai.2020200029).
- [104] *R: A Language and Environment for Statistical Computing*, R Found. Stat. Comput., R Core Team, Vienna, Austria, 2020. [Online]. Available: <https://www.R-project.org/>
- [105] Y. Roy, H. Banville, I. Albuquerque, A. Gramfort, T. H. Falk, and J. Faubert, "Deep learning-based electroencephalography analysis: A systematic review," *J. Neural Eng.*, vol. 16, no. 5, Aug. 2019, Art. no. 051001, doi: [10.1088/1741-2552/ab260c](https://doi.org/10.1088/1741-2552/ab260c).
- [106] L. Scrucca, M. Fop, T. B. Murphy, and A. E. Raftery, "mclust 5: Clustering, classification and density estimation using Gaussian finite mixture models," *R J.*, vol. 8, no. 1, pp. 289–317, 2016.
- [107] J. J. Deeks, P. Macaskill, and L. Irwig, "The performance of tests of publication bias and other sample size effects in systematic reviews of diagnostic test accuracy was assessed," *J. Clin. Epidemiol.*, vol. 58, no. 9, pp. 882–893, Sep. 2005, doi: [10.1016/j.jclinepi.2005.01.016](https://doi.org/10.1016/j.jclinepi.2005.01.016).
- [108] A. Kassambara, "ggpubr: ggplot2 based publication ready plots," Tech. Rep., 2020.
- [109] A. Liberati et al., "The PRISMA statement for reporting systematic reviews and meta-analyses of studies that evaluate healthcare interventions: Explanation and elaboration," *BMJ*, vol. 339, Jul. 2009, Art. no. b2700, doi: [10.1136/bmj.b2700](https://doi.org/10.1136/bmj.b2700).
- [110] I. Koktzoglou, R. Huang, A. L. Ong, P. J. Aouad, E. A. Aherne, and R. R. Edelman, "Feasibility of a sub-3-minute imaging strategy for ungated quiescent interval slice-selective MRA of the extracranial carotid arteries using radial  $k$ -space sampling and deep learning-based image processing," *Magn. Reson. Med.*, vol. 84, no. 2, pp. 825–837, Aug. 2020, doi: [10.1002/mrm.28179](https://doi.org/10.1002/mrm.28179).
- [111] K. C. Tezcan, C. F. Baumgartner, R. Ruechinger, K. P. Pruessmann, and E. Konukoglu, "MR image reconstruction using deep density priors," *IEEE Trans. Med. Imag.*, vol. 38, no. 7, pp. 1633–1642, Jul. 2019, doi: [10.1109/TMI.2018.2887072](https://doi.org/10.1109/TMI.2018.2887072).
- [112] T. Rohlfing, N. M. Zahl, E. V. Sullivan, and A. Pfefferbaum, "The SR124 multichannel atlas of normal adult human brain structure," *Hum. Brain Mapping*, vol. 31, no. 5, pp. 798–819, 2010, doi: [10.1002/hbm.20906](https://doi.org/10.1002/hbm.20906).
- [113] A. M. Mendrik et al., "MRBrainS challenge: Online evaluation framework for brain image segmentation in 3T MRI scans," *Comput. Intell. Neurosci.*, vol. 2015, Jan. 2015, Art. no. 813696, doi: [10.1155/2015/813696](https://doi.org/10.1155/2015/813696).
- [114] C. R. Jack et al., "The Alzheimer's disease neuroimaging initiative (ADNI): MRI methods," *J. Magn. Reson. Imag.*, vol. 27, no. 4, pp. 685–691, Apr. 2008, doi: [10.1002/jmri.21049](https://doi.org/10.1002/jmri.21049).
- [115] I. İlsgüm et al., "Evaluation of automatic neonatal brain segmentation algorithms: The NeoBrainS12 challenge," *Med. Image Anal.*, vol. 20, no. 1, pp. 135–151, Feb. 2015, doi: [10.1016/j.media.2014.11.001](https://doi.org/10.1016/j.media.2014.11.001).
- [116] F. Hashimoto, K. Ote, T. Oida, A. Teramoto, and Y. Ouchi, "Compressed-sensing magnetic resonance image reconstruction using an iterative convolutional neural network approach," *Appl. Sci.*, vol. 10, no. 6, p. 1902, Mar. 2020, doi: [10.3390/app10061902](https://doi.org/10.3390/app10061902).
- [117] K. Pawar, Z. Chen, N. J. Shah, and G. F. Egan, "A deep learning framework for transforming image reconstruction into pixel classification," *IEEE Access*, vol. 7, pp. 177690–177702, 2019, doi: [10.1109/ACCESS.2019.2959037](https://doi.org/10.1109/ACCESS.2019.2959037).
- [118] J. Zhang et al., "Compressed sensing MR image reconstruction via a deep frequency-division network," *Neurocomputing*, vol. 384, pp. 346–355, Apr. 2020, doi: [10.1016/j.neucom.2019.12.011](https://doi.org/10.1016/j.neucom.2019.12.011).
- [119] J. Zbontar et al., "fastMRI: An open dataset and benchmarks for accelerated MRI," 2018, *arXiv:1811.08839*.
- [120] C. D. Bahadir, A. Q. Wang, A. V. Dalca, and M. R. Sabuncu, "Deep-learning-based optimization of the under-sampling pattern in MRI," *IEEE Trans. Comput. Imag.*, vol. 6, pp. 1139–1152, 2020, doi: [10.1109/TCI.2020.3006727](https://doi.org/10.1109/TCI.2020.3006727).
- [121] C. A. Cocosco, V. Kollokian, R. K.-S. Kwan, G. B. Pike, and A. C. Evans, "BrainWeb: Online interface to a 3D MRI simulated brain database," *NeuroImage*, vol. 5, no. 4, p. 425, 1997.
- [122] M. V. R. Manimala, C. D. Naidu, and M. N. G. Prasad, "Sparse MR image reconstruction considering Rician noise models: A CNN approach," *Wireless Pers. Commun.*, vol. 116, no. 1, pp. 491–511, Jan. 2021, doi: [10.1007/s11277-020-07725-0](https://doi.org/10.1007/s11277-020-07725-0).
- [123] R. Souza et al., "An open, multi-vendor, multi-field-strength brain MR dataset and analysis of publicly available skull stripping methods agreement," *NeuroImage*, vol. 170, pp. 482–494, Apr. 2018, doi: [10.1016/j.neuroimage.2017.08.021](https://doi.org/10.1016/j.neuroimage.2017.08.021).
- [124] B. H. Menze et al., "The multimodal brain tumor image segmentation benchmark (BRATS)," *IEEE Trans. Med. Imag.*, vol. 34, no. 10, pp. 1993–2024, Oct. 2015, doi: [10.1109/TMI.2014.2377694](https://doi.org/10.1109/TMI.2014.2377694).
- [125] J. Mehta and A. Majumdar, "RODEO: Robust DE-aliasing autoencoder for real-time medical image reconstruction," *Pattern Recognit.*, vol. 63, pp. 499–510, Mar. 2017, doi: [10.1016/j.patcog.2016.09.022](https://doi.org/10.1016/j.patcog.2016.09.022).
- [126] B. Landman and S. Warfield, "2013 diencephalon free challenge," Tech. Rep., 2013, doi: [10.7303/syn3270353](https://doi.org/10.7303/syn3270353).
- [127] W. Qiu, D. Li, X. Jin, F. Liu, and B. Sun, "Deep neural network inspired by iterative shrinkage-thresholding algorithm with data consistency (NISTAD) for fast undersampled MRI reconstruction," *Magn. Reson. Imag.*, vol. 70, pp. 134–144, Jul. 2020, doi: [10.1016/j.mri.2020.04.016](https://doi.org/10.1016/j.mri.2020.04.016).
- [128] Y. Li, X. Cheng, and G. Gui, "Co-robust-ADMM-Net: Joint ADMM framework and DNN for robust sparse composite regularization," *IEEE Access*, vol. 6, pp. 47943–47952, 2018, doi: [10.1109/ACCESS.2018.2867435](https://doi.org/10.1109/ACCESS.2018.2867435).
- [129] D. C. Van Essen et al., "The human connectome project: A data acquisition perspective," *NeuroImage*, vol. 62, no. 4, pp. 2222–2231, Oct. 2012, doi: [10.1016/j.neuroimage.2012.02.018](https://doi.org/10.1016/j.neuroimage.2012.02.018).
- [130] Y. Han, J. Yoo, H. H. Kim, H. J. Shin, K. Sung, and J. C. Ye, "Deep learning with domain adaptation for accelerated projection-reconstruction MR," *Magn. Reson. Med.*, vol. 80, no. 3, pp. 1189–1205, Sep. 2018, doi: [10.1002/mrm.27106](https://doi.org/10.1002/mrm.27106).
- [131] B. Zufiria et al., "A feature-based convolutional neural network for reconstruction of interventional MRI," *NMR Biomed.*, Dec. 2019, Art. no. e4231, doi: [10.1002/nbm.4231](https://doi.org/10.1002/nbm.4231).
- [132] T. Eo, H. Shin, Y. Jun, T. Kim, and D. Hwang, "Accelerating Cartesian MRI by domain-transform manifold learning in phase-encoding direction," *Med. Image Anal.*, vol. 63, Jul. 2020, Art. no. 101689, doi: [10.1016/j.media.2020.101689](https://doi.org/10.1016/j.media.2020.101689).
- [133] N. Subhas et al., "Diagnostic interchangeability of deep convolutional neural networks reconstructed knee MR images: Preliminary experience," *Quant. Imag. Med. Surg.*, vol. 10, no. 9, pp. 1748–1762, Sep. 2020, doi: [10.21037/QIMS-20-664](https://doi.org/10.21037/QIMS-20-664).
- [134] A. Carass et al., "Longitudinal multiple sclerosis lesion segmentation: Resource and challenge," *NeuroImage*, vol. 148, no. 1, pp. 77–102, Mar. 2017, doi: [10.1016/j.neuroimage.2016.12.064](https://doi.org/10.1016/j.neuroimage.2016.12.064).
- [135] A. M. Sawyer et al., "Creation of fully sampled MR data repository for compressed sensing of the knee," *Tech. Rep.*, 2013.
- [136] O. Commowick, F. Cervenansky, and R. Ameli. (2016). *MSSEG Challenge Proceedings: Multiple Sclerosis Lesions Segmentation Challenge Using a Data Management and Processing Infrastructure*. Accessed: Feb. 26, 2021. [Online]. Available: <https://www.hal.inserm.fr/inserm/01397806>
- [137] Y. Dai and P. Zhuang, "Compressed sensing MRI via a multi-scale dilated residual convolution network," *Magn. Reson. Imag.*, vol. 63, pp. 93–104, Nov. 2019, doi: [10.1016/j.mri.2019.07.014](https://doi.org/10.1016/j.mri.2019.07.014).
- [138] E. Bullitt et al., "Vessel tortuosity and brain tumor malignancy: A blinded study," *Academic Radiol.*, vol. 12, no. 10, pp. 1232–1240, Oct. 2005, doi: [10.1016/j.acra.2005.05.027](https://doi.org/10.1016/j.acra.2005.05.027).
- [139] X. Qu, Y. Hou, F. Lam, D. Guo, J. Zhong, and Z. Chen, "Magnetic resonance image reconstruction from undersampled measurements using a patch-based nonlocal operator," *Med. Image Anal.*, vol. 18, no. 6, pp. 843–856, Aug. 2014, doi: [10.1016/j.media.2013.09.007](https://doi.org/10.1016/j.media.2013.09.007).
- [140] E. M. Eksioglu, "Decoupled algorithm for MRI reconstruction using nonlocal block matching model: BM3D-MRI," *J. Math. Imag. Vis.*, vol. 56, no. 3, pp. 430–440, Nov. 2016, doi: [10.1007/s10851-016-0647-7](https://doi.org/10.1007/s10851-016-0647-7).
- [141] M. A. Griswold et al., "Generalized autocalibrating partially parallel acquisitions (GRAPPA)," *Magn. Reson. Med.*, vol. 47, no. 6, pp. 1202–1210, Jun. 2002, doi: [10.1002/mrm.10171](https://doi.org/10.1002/mrm.10171).
- [142] S. G. Lingala, Y. Hu, E. DiBella, and M. Jacob, "Accelerated dynamic MRI exploiting sparsity and low-rank structure: k-t SLR," *IEEE Trans. Med. Imag.*, vol. 30, no. 5, pp. 1042–1054, May 2011, doi: [10.1109/TMI.2010.2100850](https://doi.org/10.1109/TMI.2010.2100850).
- [143] Z. Xie, L. Liu, and C. Yang, "An entropy-based algorithm with nonlocal residual learning for image compressive sensing recovery," *Entropy*, vol. 21, no. 9, p. 900, Sep. 2019, doi: [10.3390/e21090900](https://doi.org/10.3390/e21090900).
- [144] Z. Xie, L. Liu, and C. Yang, "A probabilistic model-based method with nonlocal filtering for robust magnetic resonance imaging reconstruction," *IEEE Access*, vol. 8, pp. 82347–82363, 2020, doi: [10.1109/ACCESS.2020.2991442](https://doi.org/10.1109/ACCESS.2020.2991442).
- [145] B. Wen, Y. Li, and Y. Bresler, "Image recovery via transform learning and low-rank modeling: The power of complementary regularizers," *IEEE Trans. Image Process.*, vol. 29, pp. 5310–5323, 2020, doi: [10.1109/TIP2020.2980753](https://doi.org/10.1109/TIP2020.2980753).
- [146] S. Abdullah, O. Arif, M. B. Arif, and T. Mahmood, "MRI reconstruction from sparse  $K$ -space data using low dimensional manifold model," *IEEE Access*, vol. 7, pp. 88072–88081, 2019, doi: [10.1109/ACCESS.2019.2925051](https://doi.org/10.1109/ACCESS.2019.2925051).
- [147] J. Lv, K. Chen, M. Yang, J. Zhang, and X. Wang, "Reconstruction of undersampled radial free-breathing 3D abdominal MRI using stacked convolutional auto-encoders," *Med. Phys.*, vol. 45, no. 5, pp. 2023–2032, May 2018, doi: [10.1002/mp.12870](https://doi.org/10.1002/mp.12870).
- [148] V. Antun, F. Renna, C. Poon, B. Adcock, and A. C. Hansen, "On instabilities of deep learning in image reconstruction and the potential costs of AI," *Proc. Nat. Acad. Sci. USA*, vol. 117, no. 48, pp. 30088–30095, 2020, doi: [10.1073/pnas.1907377117](https://doi.org/10.1073/pnas.1907377117).
- [149] E. Esfahani and A. Hosseini, "Compressed MRI

- reconstruction exploiting a rotation-invariant total variation discretization,” *Magn. Reson. Imag.*, vol. 71, pp. 80–92, Sep. 2020, doi: [10.1016/j.mri.2020.03.008](https://doi.org/10.1016/j.mri.2020.03.008).
- [150] L. Qiusheng, F. Xiaoyu, S. Baoshun, and Z. Xiaohua, “Compressed sensing MRI based on the hybrid regularization by denoising and the epigraph projection,” *Signal Process.*, vol. 170, May 2020, Art. no. 107444, doi: [10.1016/j.sigpro.2019.107444](https://doi.org/10.1016/j.sigpro.2019.107444).
- [151] F. Hashimoto, K. Ote, T. Oida, A. Teramoto, and Y. Ouchi, “Compressed-sensing magnetic resonance image reconstruction using an iterative convolutional neural network approach,” *Appl. Sci.*, vol. 10, no. 6, Mar. 2020, Art. no. 6, doi: [10.3390/app10061902](https://doi.org/10.3390/app10061902).
- [152] Y. Chen, Z. Fang, S.-C. Hung, W.-T. Chang, D. Shen, and W. Lin, “High-resolution 3D MR fingerprinting using parallel imaging and deep learning,” *NeuroImage*, vol. 206, Feb. 2020, Art. no. 116329, doi: [10.1016/j.neuroimage.2019.116329](https://doi.org/10.1016/j.neuroimage.2019.116329).
- [153] D. F. McGivney et al., “Magnetic resonance fingerprinting review. Part 2: Technique and directions,” *J. Magn. Reson. Imag.*, vol. 51, no. 4, pp. 993–1007, Apr. 2020, doi: [10.1002/jmri.26877](https://doi.org/10.1002/jmri.26877).